Accounting for hydrolysis in the modeling of titanium dioxide nanoparticle synthesis in laminar TiCl 4 flames

Jean-Maxime Orlac'H, Nasser Darabiha, Sebastien Candel, Denis Veynante, Benedetta Franzelli

Accounting for hydrolysis in the modeling of titanium dioxide nanoparticle synthesis in laminar $TiCl_4$ flames

Jean-Maxime Orlac'h*[,1], Nasser Darabiha[1], Sebastien Candel[1], Denis Veynante[1], and Benedetta Franzelli†[1]

[1]EM2C laboratory, CNRS, CentraleSupélec, Université Paris-Saclay, 3 rue Joliot Curie, 91192 Gif-sur-Yvette, France

July 26th 2022

Abstract

The description of TiO_2 synthesis in $TiCl_4$ flames is most often based on phenomenological models that qualitatively reproduce experimental trends in terms of final production but they do not provide chemical insights into the actual kinetic pathways. Alternatively, thermodynamically-consistent detailed $TiCl_4$ oxidation kinetics are available. However, since they have been developed under dry conditions they still need to be challenged and validated when employed for flame synthesis where the presence of water molecules may potentially activate $TiCl_4$ hydrolysis. To derive accurate chemical descriptions for TiO_2 flame synthesis, it is essential to evaluate the possible contribution of $TiCl_4$ hydrolysis. For this, numerical simulations of TiO_2 flame synthesis in laminar flames are performed in this article using different chemical descriptions for $TiCl_4$ conversion into TiO_2. Detailed oxidation kinetics neglecting hydrolysis are shown to predict an extremely slow formation of TiO_2 particles in flames when O_2 concentration is small. As a consequence, a significant underestimation of the conversion yield is observed compared to experimental evidences and to trends deduced from phenomenological models. To correct this behaviour, a new scheme is proposed by combining a detailed oxidation kinetics with a five-reaction mechanism describing the first steps of $TiCl_4$ hydrolysis. Conversion of $TiCl_4$ is found to be faster and more efficient with this new combined scheme, leading to log-normal particle size distributions in agreement with the experimental data for nanoparticles flame synthesis.

1 Introduction

Among the different techniques that are being used to produce nanoparticles, flame synthesis has received considerable attention because it allows large-scale production at low-cost of nanoparticles, with properties that may be controlled by suitably selecting flow configurations, flame structures and operating conditions [1–3]. The case of titanium dioxide synthesis is considered in the present article because it is generic, raises fundamental issues and has practical importance [4, 5]. Although flame synthesis only covers a small part of the worldwide market for pigmentary TiO_2 [6], it represents a promising alternative for the industrial

*Present address: DAAA, ONERA, 29 Avenue de la Division Leclerc, 92322 Châtillon, France

†Corresponding author: benedetta.franzelli@centralesupelec.fr

production of nanoparticles with specific properties, possibly leading to the creation of new materials with interesting characteristics. For this, an understanding of the combustion process leading to TiO_2 particles is clearly needed to optimize the corresponding flame system. However, the chemical pathways of this process are not well understood. In general, the two main pathways considered for $TiCl_4$ conversion into TiO_2 are oxidation and hydrolysis corresponding to the following global reactions:

- oxidation: $TiCl_4 + O_2 \rightarrow TiO_2 + 2Cl_2$
- hydrolysis: $TiCl_4 + 2H_2O \rightarrow TiO_2 + 4HCl$.

The relative contribution of these processes are today not clearly quantified due to the lack of detailed experimental data. Most studies focus on the size distributions, particle shape and phase composition of final products [7–13], but give little insight on the conversion kinetics. Few experiments provide estimates of $TiCl_4$ consumption rate [12, 14, 15] or normalised particle size distributions (PSD) [16, 17], but under dry conditions, where hydrolysis is absent. However, the role of hydrolysis compared to oxidation is expected to be significant in some configurations and under certain operating conditions. In specific, one expects that hydrolysis will not occur when conversion is carried out under dry conditions, such as an externally heated furnace where titanium oxide particles will be formed by $TiCl_4$ oxidation. On the contrary, flame synthesis implying hydrocarbon combustion will naturally yield water vapor so that hydrolysis of $TiCl_4$ is expected to contribute to TiO_2 formation. However, the contribution of $TiCl_4$ hydrolysis during TiO_2 flame synthesis is still not clear. From the experimental point of view, it is difficult to discriminate the hydrolysis from the oxidation pathway. However, it is worth noting that in the 1980's many combustion experiments were carried out using $TiCl_4$ as a diagnostic tool to visualize flame front [18, 19], where H_2O is generated. In the corresponding publications, it was commonly admitted that the $TiCl_4$ precursor would react with the water vapor in the flame front almost instantaneously allowing its visualization by detecting the laser light scattered by the TiO_2 solid particles. From a numerical point of view, Heine and Pratsinis [20] considered both oxidation and hydrolysis pathways to investigate the effect of $TiCl_4$ concentration on the characteristics of the final TiO_2 agglomerates. However, since the two paths were not considered in combination, it is not possible to know whether hydrolysis or oxidation dominated. Thermodynamic calculations of Akhtar *et al.* [21] for reactor furnaces showed that the oxidation process is dominant when the water vapor concentration is low. At the same time, recent thermodynamic data show that hydrolysis should be considered in flames since concentrations of hydrogen-containing species are not negligible [22].

Overall, experimental evidences and numerical data indicate that, in order to dispose of an accurate kinetic description for TiO_2 formation valid both in dry conditions and in flames, both oxidation and hydrolysis of $TiCl_4$ should be accounted for to quantify their respective contributions to TiO_2 synthesis. In literature, two main approaches exist to describe the kinetic modeling of TiO_2 production from $TiCl_4$ decomposition, but none of them described hydrolysis. The first relies on state-of-the-art phenomenological models developed by fitting the reaction parameters to reproduce experimental data, such as the $TiCl_4$ consumption rate [14]. The second employs detailed kinetic schemes for $TiCl_4$ oxidation under dry conditions consistent with thermodynamic equilibrium theory [23, 24]. These detailed models have been considered for the simulation of TiO_2 turbulent flame synthesis [25, 26] but the absence of hydrolysis pathways is expected to have an impact on their predictions that needs to be quantified.

As a first step toward a better description of combustion processes in TiO_2 synthesis, the first objective of this work is to account for hydrolysis in Section 2.1 by adding to a detailed oxidation scheme a five-step reaction mechanism for $TiCl_4$ hydrolysis, in analogy with the recent works performed for titanium tetraisopropoxide (TTIP) flames [27, 28]. Then, the second objective is to examine the role of hydrolysis on laminar flame synthesis of TiO_2 nanoparticles by evaluating the possible inaccuracies of a kinetic mechanism when only $TiCl_4$ oxidation is considered. For this, the performances of the new model are evaluated in Sec. 3 in four configurations including a furnace reactor, a 1-D laminar freely-propagating

premixed flame, a counterflow diffusion flame and a 2-D nonpremixed co-flow flame. Due to the limited availability of experimental data in such canonical test cases, the performances of the detailed oxidation model and of the new model are evaluated in terms of global quantities, such as the conversion yield, in comparison with results derived from the phenomenological description, which is widely used to simulate TiO_2 synthesis in dry conditions and flames seeded with $TiCl_4$. Experimental data are also considered when available. Conclusions drawn in Section 4 also include perspectives and in particular point out the need for experiments that will not only focus on final products but that would also provide information on the evolution of Ti-species.

2 Modeling TiO_2 synthesis in flames seeded with $TiCl_4$

Conversion of $TiCl_4$ precursor species in flames produces titanium oxide solid particles containing from several tens to several thousands of Ti atoms. Liquid $TiCl_4$ is classically used in applications but, for simplicity, it is convenient in this work to consider operating conditions that guarantee a prevaporized state for $TiCl_4$, i.e. an initial temperature higher than its evaporation temperature $T = 410$ K. In the following, $TiCl_4$ flames will stand for methane flames seeded with gaseous $TiCl_4$. To describe them, different submechanisms have to be included for gaseous and solid phases, which are schematically represented in Fig. 1. For the gaseous phase, the kinetic description has to account for three blocks: methane oxidation, $TiCl_4$ conversion into TiO_2 and chlorination of methane. The methane oxidation and chlorination processes are here described using the reduced mechanism from Mehta et al. [29], which accounts for 37 species and 129 reactions. For the description of the $TiCl_4$ conversion into TiO_2, three different submechanisms will be considered separately in this work: a phenomenological reaction scheme (PRS) [14], a detailed oxidation scheme (DOS) [29] and a new combined oxidation and hydrolysis scheme (OHS). These three submechanisms will be described in Sec. 2.1. A mixture-averaged model is assumed for the diffusion coefficients of the gaseous species. Results on particle volume fraction could be directly derived from the gaseous $TiO_{2(g)}$ mass fraction. However, a more detailed characterization of nanoparticles can be obtained by adding a solid phase description to the simulations. For this, once gaseous $TiO_{2(g)}$ is produced, an infinitely fast nucleation process is assumed to form the first solid particles $TiO_{2(s)}$. In general, the nucleated particles are treated as monomers [30]. Here, following the recommendations of Mehta et al. [25], five Ti atoms are required to constitute a freshly nucleated solid particle. The solid phase is then represented using a sectional model and the particle size distribution (PSD) is deduced therefrom. Thirty sections are considered [31]. The mass and enthalpy conservation formulation proposed in Orlac'h et al. [32] is retained. The particles diffusion velocity involves a thermophoretic contribution [33, 34] and a diffusion term induced by concentration gradients. The particles diffusion coefficients are computed in the free molecular regime. The particle thermophoresis velocity is taken from Waldmann [33]. The nanoparticles dynamics involve only nucleation and coagulation. By neglecting sintering it is implicitely assumed that the corresponding characteristic time is negligible with respect to the coagulation time. However this assumption may not be true in the whole flame [3] and a more elaborate modeling might be needed to account for coagulation and sintering competition in the sectional framework, i.e. non-spherical particles, which is left for future work. For simplicity, in the present work, we assume that particles are spherical and that coagulation between two spherical particles gives rise to a single spherical particle so that the description of sintering is not needed. Since the Brownian coagulation leads to a self-preserving size distribution, the conclusions on the particle size density (PSD) are not expected to be notably affected by this assumption. The coagulation rate is expressed in a transition regime between the free molecular and the continuum regimes [32] through the collision frequency $\beta_{i,j}$ between a particle of volume v_i and a particle of volume v_j as:

$$\beta_{i,j} = \frac{\beta_{i,j}^{\mathrm{fm}} \beta_{i,j}^{\mathrm{c}}}{\beta_{i,j}^{\mathrm{fm}} + \beta_{i,j}^{\mathrm{c}}} \approx \min(\beta_{i,j}^{\mathrm{fm}}, \beta_{i,j}^{\mathrm{c}}) \tag{2.1}$$

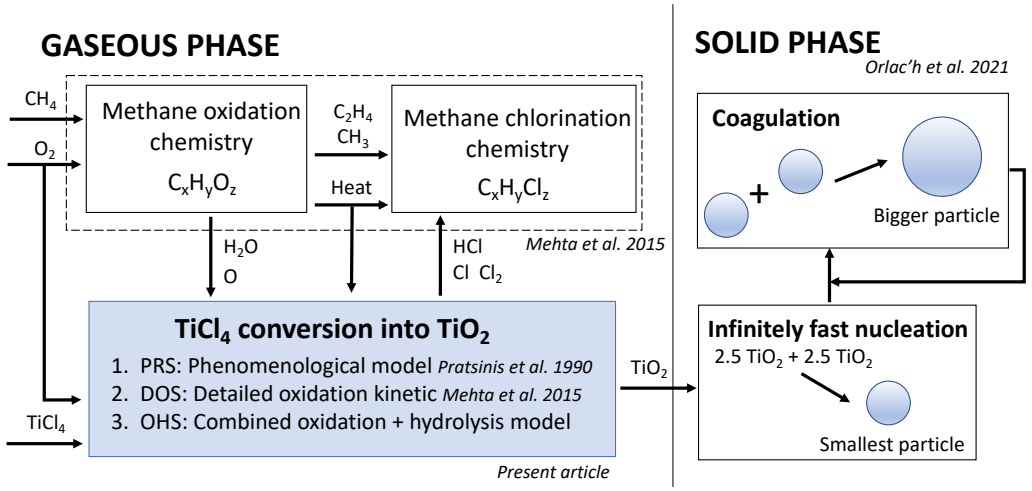

Figure 1 – Schematic representation of the models considered in this work for the simulation of TiO_2 synthesis in $TiCl_4$ flames.

with the collision frequency for free molecular regime (superscript fm) and the continuum regime (superscript c) respectively given by:

$$\begin{aligned} \beta_{i,j}^{\mathrm{fm}} &= \frac{1}{2}\,\epsilon_{\mathrm{coag}} \left(\frac{2\pi k_B T}{\rho_{\mathrm{s}}}\right)^{1/2} \sqrt{\frac{1}{v_i}+\frac{1}{v_j}}\,(d_{c,i}+d_{c,j})^2 \\ \beta_{i,j}^{\mathrm{c}} &= \frac{2k_B T}{3\mu}\,(d_{c,i}+d_{c,j})\left(\frac{\mathrm{C}_i}{d_{c,i}}+\frac{\mathrm{C}_j}{d_{c,j}}\right) \end{aligned} \tag{2.2}$$

where $\epsilon_{\mathrm{coag}} = 2.2$ is an amplification factor due to Van der Waals interactions [31] and μ is the gas dynamic viscosity given by Sutherland's formula [35] $\mu = C_1 T^{3/2}/(T + C_2)$. The coefficients C_1 and C_2 are the Sutherland coefficients, and C_j is the Cunningham corrective coefficient for a particle of volume v_j [36]:

$$\mathrm{C}_j = 1 + 1.257\,\mathrm{Kn}_j = 1 + 1.257\,\frac{2l_{\mathrm{gas}}}{d_{c,j}} \tag{2.3}$$

where Kn_j is the Knudsen number. $d_{c,j}$ is the collisional diameter of a particle of volume v_j equal to the particle diameter since we consider spherical particles. Finally, $l_{\mathrm{gas}} = k_B T/(\sqrt{2}\pi d_{\mathrm{gas}}^2 p)$ is the mean free path of the gaseous phase, where k_B is the Boltzmann constant, $d_{\mathrm{gas}} = 0.2$ nm is the diameter of a typical gas particle and p is the pressure.
Surface growth is not considered here but it has been verified by applying the surface growth model of Ghoshtagore [30, 37–40] that its effects on nanoparticles global quantities and size distributions is negligible compared to nucleation and coagulation processes in all the 1-D cases examined in this article. When only nucleation and coagulation are considered, there is no backward coupling between the solid and gaseous phases so that, if needed, these two phases can be simulated separately [41].

2.1 Models for conversion of $TiCl_4$ into TiO_2

As already indicated, experimental data on the relative contribution of $TiCl_4$ oxidation and hydrolysis on TiO_2 production in flames are today scarce. $TiCl_4$ hydrolysis is generally admitted to occur even at room temperature [42] and the conversion of $TiCl_4$ into TiO_2 is usually considered to be fast [14, 18, 43] since:

- A high conversion yield (60 % to 95 % depending on the oxidizer concentration) is observed in co-flow diffusion flames [43].

- Particle sizes rapidly reach a self-similar log-normal distribution [5, 7, 41, 44, 45], meaning that the conversion of $TiCl_4$ into TiO_2 is a quick process leading to a fast nucleation of solid particles, which are then only subjected to coagulation.

Although no information is given about the relative oxidation/hydrolysis contribution in TiO_2 production, experimental data indicate that the kinetics of $TiCl_4$ conversion into TiO_2 is extremely efficient, pleading in favour of a fast conversion kinetics when considering TiO_2 production in flames. It is then important to verify whether the submechanism for conversion of $TiCl_4$ into TiO_2 retrieves these qualitative experimental observations. Two main approaches can be found in literature:

- Empirical phenomenological reaction scheme (PRS) such as the model of Pratsinis et al. [14], whose reaction progress rate Q_{global} [mol.cm^{-3}.s^{-1}] reads as:

$$Q_{\text{global}} = \text{A}_{\text{global}} \exp\left(-\text{E}_{\text{global}}/(RT)\right)[X_{\text{TiCl}_4}] \tag{2.4}$$

  with $\text{A}_{\text{global}} = 8.26 \cdot 10^4$ s^{-1} the pre-exponential factor, $R = 8.31$ J.mol^{-1}.K^{-1} is the gas constant, $\text{E}_{\text{global}} = 88.8$ kJ.mol^{-1} the activation energy, T the gas temperature and $[X_{\text{TiCl}_4}]$ the molar concentration of $TiCl_4$. The rate constants were fitted to reproduce the experimental consumption of $TiCl_4$ obtained in an externally heated tubular reactor for a $TiCl_4/O_2/Ar$ mixture, i.e. under dry conditions. This global reaction is widely used in numerical simulations of TiO_2 nanoparticle formation [17, 20, 30, 38–40]. Initial numerical calculations based on this model were aimed at investigating conditions representative of the chloride process in externally heated dry conditions [30, 38, 39], and analyzing the sensitivity of the PSD to global parameters such as surface growth or turbulence intensity with no comparisons with experimental data. This model was more recently validated in co-flow diffusion flames in terms of nanoparticle volume fractions and particle size distributions, at least for particle sizes larger than 35 nm [41]. One may identify two drawbacks when using a PRS model:

  1. The reaction progress rate depends only on $TiCl_4$ concentration and temperature, i.e. this phenomenological model guarantees a fast conversion of $TiCl_4$ into TiO_2 when a sufficiently high temperature is reached without any details on the real chemical pathways.
  2. Such global reaction rates may lead to some numerical issues due to a too simple description of the chemical pathways. Indeed, Q_{global} can be non-zero even for zero O_2 concentration, leading then to negative O_2 mass fraction and/or non-conservation of O atoms.

  However, this model is today considered as a good estimator of experimental trends for the final products and is widely used to simulate TiO_2 synthesis in $TiCl_4$ flames [17, 20, 30, 38–40]. It will be used in the following to evaluate the performances of the other models in the absence of experimental data on laminar flames since it represents the state-of-the-art in terms of TiO_2 modeling in $TiCl_4$ flames.

- Detailed oxidation kinetics (DOS). A detailed kinetic scheme for the gas-phase reactions of $TiCl_4$ with O_2 was developed by West et al. [23] based on density functional theory calculations. The model comprises 30 species and 66 reactions and its reaction rates are consistent with thermodynamic equilibrium theory. It agrees reasonably well with the phenomenological description in terms of $TiCl_4$ consumption rate as a function of temperature under dry conditions [24]. However, to our knowledge, such detailed oxidation kinetic schemes have not been validated in terms of nanoparticle volume fraction or number density in flames. Detailed mechanisms have mostly been applied to $TiCl_4$-O_2 mixtures externally heated [46–48] but these conditions are not fully representative of nanoparticle flame synthesis since water molecules are absent. More recent studies [46, 48] have used this oxidation mechanism to calculate the $TiCl_4$ consumption rate and compare numerical predictions with the plug flow reactor data of Pratsinis et al. [14]. These works illustrate the

Reactions from Wang et al. (2010)	Rate constants $\tilde{k}$ T = 298K	T = 700K	T = 1500K
R1: $TiCl_4$+ $H_2O \rightarrow TiCl_3OH(g) + HCl(g)$	2.0×10^{-3}	3.0×10^{2}	5.0×10^{4}
R2: $TiCl_3OH(g) + H_2O(g) \rightarrow TiCl_2(OH)_2(g) + HCl(g)$	5.1×10^{-4}	3.4×10^{1}	4.3×10^{3}
R3: $TiCl_2(OH)_2(g) + H_2O(g) \rightarrow TiCl(OH)_3(g) + HCl(g)$	4.8×10^{-3}	8.4×10^{1}	6.1×10^{3}
R4: $TiCl(OH)_3(g) + H_2O(g) \rightarrow Ti(OH)_4(g) + HCl(g)$	3.5×10^{-3}	1.3×10^{2}	1.3×10^{4}

Table 1 – Reaction rate constants $\tilde{k} = kN_a^{-1}$ [cm^3 $molecule^{-1}$ s^{-1}] for the first four reaction steps for $TiCl_4$ hydrolysis up to $Ti(OH)_4$ for three temperatures from Wang et al. [49].

sensitivity of the process to the model, e.g. mixing efficiency, nanoparticle fractality, process temperature or flow rate, but without validation in terms of nanoparticle volume fraction and PSDs since the corresponding data were not available. Mehta et al. [25, 26] compared the performances of a detailed oxidation scheme based on the work of West et al. [24] with the phenomenological model in two co-flow diffusion flames investigated by Pratsinis et al. [13]. In these cases, the detailed oxidation model correctly predicted the experimental $TiCl_4$ consumption. However, the TiO_2 formation rate was approximately 10 times slower with the detailed oxidation mechanism than with the phenomenological scheme that was previously validated on experimental data, indicating that the detailed oxidation model underestimates TiO_2 production in flames. To summarize, in contrast with the phenomenological model, this mechanism is expected to accurately describe the $TiCl_4$ oxidation kinetics but the conversion yield is too slow when the water vapor concentration is not negligible.

In the present work, the global mechanism of Pratsinis et al. [14] and the $TiCl_4$ oxidation scheme of Mehta et al. [29], which accounts for 14 species and 36 reactions, will respectively serve as PRS and DOS models for the conversion of $TiCl_4$ into TiO_2. In addition, a third submechanism is proposed in the following to include the first steps of hydrolysis kinetics into a DOS description.

Accounting for $TiCl_4$ hydrolysis kinetics

Although experimental evidence indicates that the hydrolysis kinetics may play an important role in TiO_2 nanoparticles production in $TiCl_4$ flames, only very few studies consider the development of corresponding detailed schemes. Progress has only recently been made in the understanding of the hydrolysis kinetics. Totton *et al.* [22] have derived a self-consistent thermochemistry for the conversion of $TiCl_4$ in methane flames, accounting for both oxygen and water. Their data only concern thermochemical equilibrium and information on the chemical pathways are not provided. In parallel, Wang et al. [49] demonstrate using potential energy surface calculations and Rice-Ramsperger-Kassel-Marcus theory that the hydrolysis of $TiCl_4$ does not result in the formation of $TiOCl_2$ and HCl, nor TiO_2 and HCl as predicted by the global reaction due to the substantial endothermicities associated with the formation of gaseous TiO_2. Therefore, intermediate Ti- species are expected to be formed by the hydrolysis process. For this, they provided the first four $TiCl_4$ hydrolysis reactions up to the production of gaseous $Ti(OH)_4$ together with their reaction rates $\tilde{k}$ [$cm^3 molecule^{-1} s^{-1}$] at three reference temperatures (T = 298, 700, 1500 K), as listed in Table 1.

We here propose to add to the $TiCl_4$ oxidation kinetics model assembled by Mehta et al. [29] a hydrolysis submechanism accounting for:

- $TiCl_4$ hydrolysis into $Ti(OH)_4$ via the chemical pathways identified by Wang et al. [49].
- The bimolecular collision of two $Ti(OH)_4$ molecules into TiO_2, based on the model of Lindberg et al. [50] for TTIP flames.

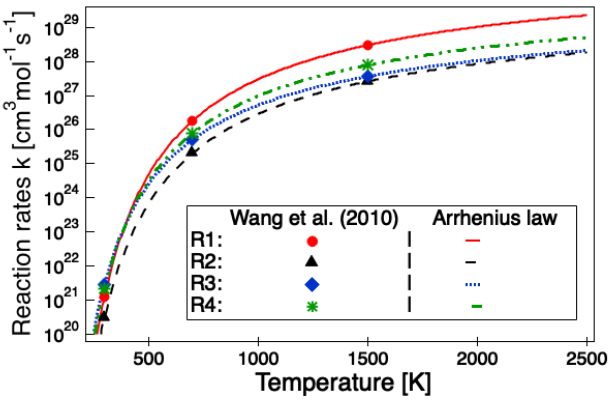

Figure 2 – Comparison of the reaction rates R1-R4 using the Arrhenius law (lines) with the available data from Wang *et al.* [49].

Concerning $TiCl_4$ hydrolysis into $Ti(OH)_4$, in order to dispose of a kinetic mechanism, the reaction rates $k = N_a\tilde{k}$ [$cm^3mol^{-1}s^{-1}$] need to be expressed in the form of an Arrhenius law: $k = \boldsymbol{A}T^{\beta}\exp(-E/(RT))$, where N_a is the Avogadro number, $\boldsymbol{A}$ is the pre-exponential factor, β accounts for temperature dependency and E is the activation energy. For this, we fit the available data on reaction rates provided by Wang *et al.* [49] and presented in Table 1 with a least squares linear regression to obtain the values for $\boldsymbol{A}$, β and E for each reaction. The reaction parameters obtained in this way are provided in Table 2. A comparison of the reaction rates R1-R4 using the Arrhenius law (lines) with the available data from Wang et al. [49] (symbols) is provided in Fig. 2. The reaction parameters correctly reproduce the evolution of the reaction rate constants with temperature.

Once $TiCl_4$ is converted into $Ti(OH)_4$, an additional step is introduced to describe the formation of TiO_2 in analogy with the model provided in [50] for TiO_2 synthesis in TTIP flames. $Ti(OH)_4$ species is then considered as the main intermediate species leading to the formation of TiO_2 as the results of a bimolecular collision of two $Ti(OH)_4$ molecules. In order to provide a consistent description with the phenomenological and the detailed oxidation model, we add a fifth reaction to the model in Table 2 by rewriting the free molecular collision kernel used in [50] in the form of an Arrhenius law.

Hydrolysis process is probably more complex and involves many more intermediate species than the five-step mechanism proposed here. However, this can be considered as a first step forward in the description of $TiCl_4$ hydrolysis in view of its use for numerical simulations of industrial systems. In addition, the principle aim here is to analyze whether the hydrolysis pathway can dominate the more standard oxidation pathway in $TiCl_4$ flames. For this, the five-steps hydrolysis submechanism of Table 2 is added to the

Reaction	$\boldsymbol{A}$ **[$cm^3.mol^{-1}.s^{-1}$]**	β	E **[cal/mol]**	**Ref.**
R1: $TiCl_4$+ $H_2O \rightarrow TiCl_3OH(g) + HCl(g)$	$1.44 \cdot 10^{27}$	0.941	11 467	[49]
R2: $TiCl_3OH(g) + H_2O(g) \rightarrow TiCl_2(OH)_2(g) + HCl(g)$	$4.01 \cdot 10^{25}$	1.053	10 528	[49]
R3: $TiCl_2(OH)_2(g) + H_2O(g) \rightarrow TiCl(OH)_3(g) + HCl(g)$	$5.68 \cdot 10^{25}$	0.992	9201	[49]
R4: $TiCl(OH)_3(g) + H_2O(g) \rightarrow Ti(OH)_4(g) + HCl(g)$	$1.02 \cdot 10^{26}$	1.049	9926	[49]
R5: $Ti(OH)_4(g) + Ti(OH)_4(g) \rightarrow 2\ TiO_2(g) + 4\ H_2O$	$5.23 \cdot 10^{12}$	0.5	0	[27]

Table 2 – Five-step $TiCl_4$ hydrolysis submechanism combined to the Mehta et al. [29] mechanism in the OHS chemical scheme.

oxidation kinetics model proposed by Mehta et al. [29] so that the resultant mechanism, referred to as the oxidation and hydrolysis scheme (OHS), will account for both oxidation and hydrolysis of $TiCl_4$. It should be mentioned that thermodynamic equilibrium calculations showed that the PRS, DOS and OHS schemes provide identical TiO_2 equilibrium concentration for a given initial state.

3 Model calculations in reference configurations

The performances of three different submechanisms for $TiCl_4$ conversion are considered in the following: the PRS model of Pratsinis et al. [14], the DOS scheme of Mehta et al. [29] and the new OHS model described above. It should be noticed that experimental results in laminar flames where oxidation and hydrolysis are expected to occur are available in literature [13]. Unfortunately, they are not easy to use for the validation of the proposed hydrolysis model and of the numerical strategy retained here for two reasons. First, in [13] effects of oxidation and hydrolysis are characterized in terms of particle properties, such as rutile/anatase fraction or surface area. Unfortunately, the numerical determination of these properties will require more sophisticated models compared to those used in the present analysis. This is so because, to our knowledge, there is no simple model for distinguishing rutile and anatase forms. The surface area could be described by accounting for the fractal nature of the aggregates but the description of such properties is out of the scope of the present work. Second, the experimental characterization of the titanium dioxide powders (including primary particle size) is obtained by sampling the powders far downstream the flame in a position that is not easily estimated and might reduce the precision of the comparison between experimental and numerical data. It was therefore considered preferrable to provide a first validation of the numerical approach in the case of a furnace reactor in Sec. 3.1, where TiO_2 nanoparticles are produced by heating without flame so that no hydrolysis occurs. For this configuration, the DOS was already validated and experimental data are available. Then, the role of hydrolysis will be evaluated by examining numerical results for canonical 1-D freely propagating premixed flames and 1-D counterflow diffusion flames in Secs. 3.2 and 3.3. Results from the phenomenological model will provide predictions of experimental trends on final products. Finally, in Sec. 3.4, co-flow flames will be investigated to characterize TiO_2 nanoparticles flame synthesis in a more realistic configuration. As already indicated, the description for the methane oxidation and chlorination as well as for the solid phase is identical in all simulations. All simulations have been performed using the Regath code [51], except for the 2-D co-flow flame.

3.1 Furnace reactor

The furnace reactor configuration by Nakaso et al. [15], schematically presented in Fig. 3a, is simulated to verify that the general trends of the phenomenological model and of the detailed oxidation kinetics, which have been developed under dry conditions, are similarly retrieved by the new OHS model in the case of a $TiCl_4$-N_2-O_2 mixture heated externally, i.e. in a dry configuration. The experimental injection of $TiCl_4$ in an O_2/N_2 mixture flowing inside a heated tube is numerically described as a 1-D flow. The experimental temperature profile presented in Fig. 3b is prescribed. The N_2 and O_2 mole fractions are slightly less than 75% and 25%, respectively. The $TiCl_4$ mole fraction is $2 \cdot 10^{-5}$. The flow rate is $2.74 \cdot 10^{-2}$ g.cm^{-2}.s^{-1}.

Figure 4a shows the particle size distribution (PSD) obtained by Nakaso et al. [15] using a trivariate (diameter/volume/surface) sectional model coupled with a PRS model for $TiCl_4$ conversion. Results at different axial positions are presented and compared to the experimental PSD, which is measured downstream of the furnace exit. Experimental data provide indications on mobility diameters of aggregates and on primary particle diameters. These two features are not available in the present numerical model, so that the volume equivalent diameters from the simulations are directly compared to the experimental mobility diameters of aggregates. Discrepancies between the measured distribution and those calculated at x = 1.5 m by Nakaso et al. [15] were explained by the fact that the experimental furnace tube length was equal to 1.5 m, but the nanoparticles detection systems was located further downstream at an unknown

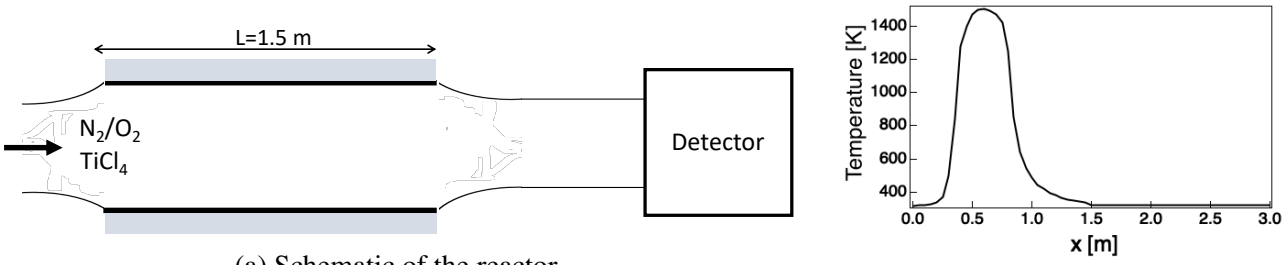

(a) Schematic of the reactor.

(b) Furnace temperature profile.

Figure 3 – Schematic of the furnace configuration from Nakaso *et al.* [15]. The gas temperature profile corresponds to the case where the furnace wall temperature is T_f = 1473 K (1200° C in [15]).

distance from the outlet. For this reason, we have presented in Figs. 4b-4d the PSD results obtained with the three $TiCl_4$ conversion mechanisms also at an arbitrary distance of x = 2.75 m to show how the PSD evolves on the way to the detection system. The three different models show similar features. The PSD shape can be easily linked to the processes governing nanoparticle production: the first peak is governed by the nucleation process, while the coagulation is responsible for the second. The phenomenological model of Fig. 4b presents a quick transition in the PSD shape from a bi-modal shape (for $x < 58$ cm), characterized by the presence of small nuclei particles and already coagulated bigger particles, to a log-normal shape (for $x > 125$ cm) mainly corresponding to big coagulated particles. As expected, these results of the PRS model are in agreement with those reported in [15] (Fig. 4a), since they both rely on a phenomenological $TiCl_4$ model. On the contrary, the DOS and the OHS models present a slower PSD transition with a high concentration of small nuclei particles at x = 92 cm. Results from these two descriptions exhibit identical trends as this case corresponds to a dry configuration in which no hydrolysis is expected. Overall, the results of the different schemes are not in contradiction with the experimental data and can be considered validated within the limits of the information available.

3.2 1-D premixed flames

One-dimensional laminar freely-propagating premixed flames are one of the simplest fundamental configurations for the characterization of combustion processes. Therefore, a 1-D premixed laminar $TiCl_4/CH_4$/air flame at atmospheric pressure, schematically presented in Fig. 5, is now considered to investigate TiO_2 flame synthesis. An inlet temperature of 500 K, higher than the evaporation temperature of $TiCl_4$, is assumed so that $TiCl_4$ is injected in gaseous form. The mass fraction of $TiCl_4$ at injection is $Y^{\text{in}}_{\text{TiCl}_4}$ =5 %.

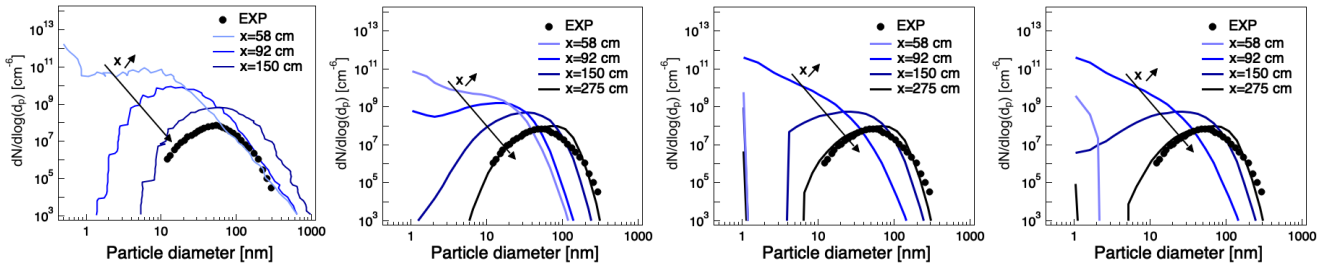

(a) Nakaso et al. [15] (b) PRS model (c) DOS model (d) OHS kinetics

Figure 4 – Comparison of simulations with experimental measurements in the configuration of Nakaso *et al.* [15] of Fig. 3.

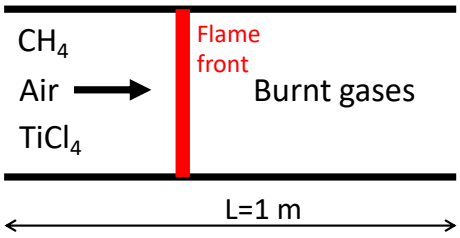

Figure 5 – Schematic of 1-D premixed flame.

Two equivalence ratios ϕ have been considered: a lean flame (ϕ = 0.6), assuring a high O_2 concentration in the burnt products, and a stoichiometric flame (ϕ = 1.0) to investigate a case with a much lower O_2 concentration in the burnt products.

The two flame structures are plotted in Fig. 6 using the OHS submechanism. The reaction zone, here defined as the zone where the CH_4 consumption rate is higher than 1% of its maximum value, is visualized in grey and it is used to scale the axial coordinate so that x = 0 mm corresponds to the beginning of the reaction zone. The reaction zone ends at $x \approx$0.65 mm and 0.4 mm for ϕ = 0.6 and 1, respectively, and it is followed by a post-flame zone. Upstream the reaction zone (x < 0 mm), a preheat zone can be identified where diffusion controls temperature and intermediate species profiles. Simulations have also been performed using PSR and DOS models. Only small discrepancies in the major species are observed for the three submechanisms (results not shown), meaning that the methane oxidation process is only slightly affected by the $TiCl_4$ conversion mechanism in premixed configurations.

In Fig. 6, both H_2O and O_2 species are found in the preheat, reaction and post-flame zones, so that $TiCl_4$ oxidation and hydrolysis are expected to occur in the same region in both cases. Figure 7 displays mole fractions of $TiCl_4$ and solid $TiO_{2(s)}$ particles as a function of the axial position for the three submechanisms and the two equivalence ratios. The mole fraction of solid $TiO_{2(s)}$ is deduced from the nanoparticle volume

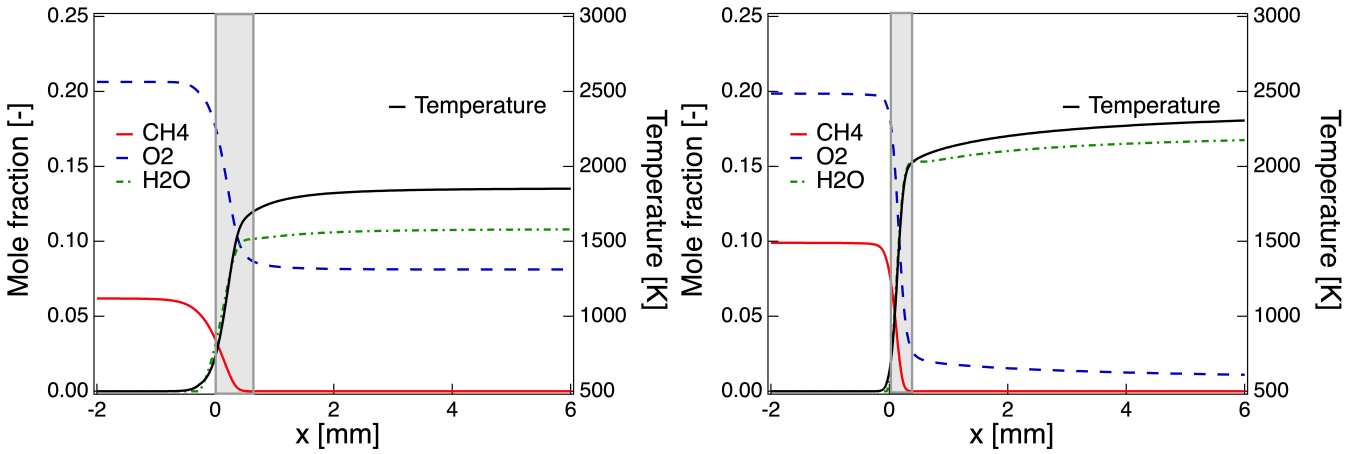

(a) Equivalence ratio ϕ = 0.6.

(b) Equivalence ratio ϕ = 1.0.

Figure 6 – Temperature and main species profiles of laminar freely-propagating premixed CH_4/air flame for two equivalence ratios ϕ = 0.6 and ϕ = 1.0. The inlet temperature is 500 K and the inlet $TiCl_4$ mass fraction is 5 %. The grey region identifies the reaction zone. Results correspond to the simulation using the OHS model.

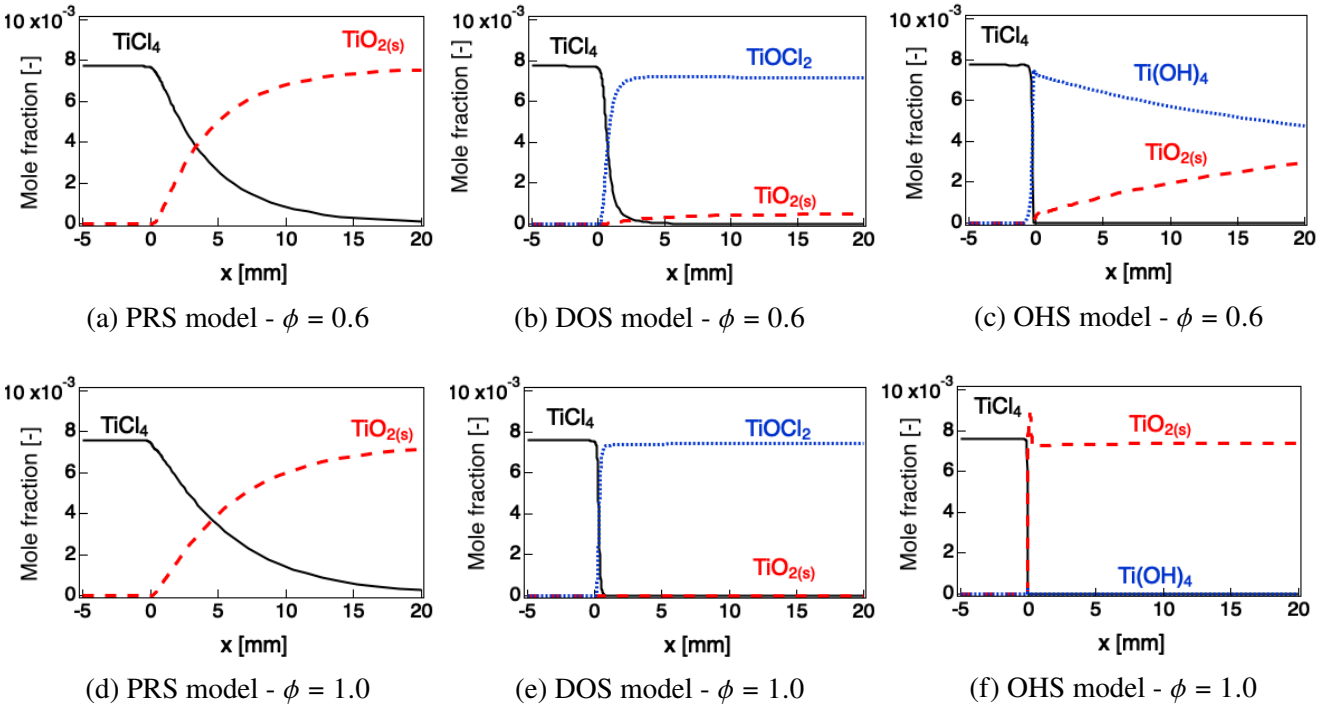

(a) PRS model - $\phi = 0.6$ (b) DOS model - $\phi = 0.6$ (c) OHS model - $\phi = 0.6$

(d) PRS model - $\phi = 1.0$ (e) DOS model - $\phi = 1.0$ (f) OHS model - $\phi = 1.0$

Figure 7 – Ti-species results using the PRS, the DOS and the OHS mechanisms in the 1-D premixed CH_4/air flames of Fig. 6.

fraction f_v:

$$X_{TiO_2(s)} = \frac{\rho_s}{\rho}\frac{\overline{W}}{W_{TiO_2}} f_v \tag{3.1}$$

where $\overline{W}$ is the mixture-averaged molar mass, $W_{TiO_2} = 79,866$ g/mol is the molar mass of TiO_2, $\rho_s = 4$ g/cm^3 is the titanium dioxide nanoparticle density and ρ is the gas mixture density.

In Figs. 7a and 7d, the phenomenological model predicts a complete consumption of $TiCl_4$ within a few centimeters from the flame front for both equivalence ratios. When considering the DOS and the OHS models an even faster $TiCl_4$ consumption rate is observed. This is consistent with the experimental data, reporting short time scales for $TiCl_4$ consumption. In order to quantify it, a characteristic time scale τ_k^{PRS} for the k^{th} species is estimated using the results obtained with the phenomenological PRS model as a reference:

$$\tau_k^{PRS} = \frac{\max(\rho Y_k)}{\max(W_k|\dot{\omega}_k|)} \tag{3.2}$$

where Y_k, W_k and $\dot{\omega}_k$ are the k^{th} species mass fractions, molar mass and net molar production rate per unit volume, respectively. The flame characteristic time τ is based on methane information, used to track the reaction zone, using the phenomenological PSR model: $\tau = \tau_{CH4}^{PRS}$. The TiO_2 production time for PRS model is identical to the $TiCl_4$ destruction time: $\tau_{TiCl_4}^{PRS} = \tau_{TiO_2}^{PRS}$, since the phenomenological model describes a global conversion of $TiCl_4$ into TiO_2.

The characteristic times for the DOS and the OHS models are obtained as:

$$\tau_k^i = \tau_k^{PRS}\frac{\max(|\dot{\omega}_k^{PRS}|)}{\max(|\dot{\omega}_k^i|)} \quad \text{for } i = \text{DOS, OHS.} \tag{3.3}$$

and compared in Table 3 with respect to flame time τ. The $TiCl_4$ consumption time scale strongly depends on the kinetic mechanism: a time scale of the same order of magnitude of the flame time scale τ is observed

Equivalence ratio	Flame time τ	$TiCl_4$ consumption τ_{TiCl_4}			TiO_2 production τ_{TiO_2}		
		PRS	DOS	OHS	PRS	DOS	OHS
0.6	0.95 ms	22 τ	3.74 τ	0.242 τ	22 τ	314 τ	31.02 τ
1.0	0.167 ms	53.3 τ	1.6 τ	0.13 τ	53.3 τ	15082 τ	0.13 τ

Table 3 – Characteristic time-scales for flame (CH_4), $TiCl_4$ consumption rate and TiO_2 production rate using the three submechanisms in configuration of Fig. 6.

when using the DOS model, whereas the $TiCl_4$ consumption process is longer/shorter of one order of magnitude when considering the PRS/OHS mechanism.

With the phenomenological model, the consumed $TiCl_4$ is directly converted into TiO_2 by construction (Figs. 7a and 7d). On the contrary, intermediate species are predicted with both the DOS and the OHS models. For this, one observes that only a small quantity of $TiCl_4$ is converted into TiO_2 at the scale of the flame when the DOS kinetics is used (Fig. 7b). TiO_2 production with the DOS model is even smaller when considering the stoichiometric case (Fig. 7e), which is less favourable to the oxidation pathways since the O_2 concentration is smaller than for $\phi = 0.6$. This indicates that the oxidation pathway is quite slow compared to the characteristic flame time ($\tau^{DOS}_{TiO_2} \approx 300\tau$ and 15000τ for $\phi = 0.6$ and $\phi = 1.0$, respectively). These results do not contradict the findings reported in [46, 48] in terms of fast $TiCl_4$ consumption rate. Indeed, the $TiCl_4$ consumption to produce $TiOCl_2$ is actually faster in the DOS model than in the PRS model for both equivalence ratios. However, the conversion of $TiOCl_2$ and other Ti-containing intermediates into TiO_2 is too slow to yield a significant conversion rate at the flame scale. This is consistent with the results in [26], where the DOS kinetics is found to be much slower compared to the PRS description in terms of TiO_2 production, even if $TiCl_4$ consumption is quite fast. For this reason, it is more relevant to look at the final product characteristics, i.e. particle size distributions and global properties, than to examine the $TiCl_4$ consumption when evaluating the performances of the different mechanisms. When considering a long computation domain (L=10 m), the TiO_2 mole fraction for the $\phi = 0.6$ case slowly increases up to half the $TiCl_4$ mole fraction at injection with the DOS model (not shown). On the contrary, for $\phi = 1.0$, the mole fraction of TiO_2 is still negligible at 10 meters since $\tau^{DOS}_{TiO_2}(\phi = 1.0)$ is extremely long.

Results with the OHS model are presented in Figs. 7c and 7f. For $\phi = 0.6$, $TiCl_4$ is rapidly converted into $Ti(OH)_4$ via hydrolysis reactions R1-R4 of Table 2 but its subsequent conversion into TiO_2 via reaction R5 is slower so that TiO_2 production is not complete at x=20 mm ($\tau^{OHS}_{TiO_2}(\phi = 0.6) \approx 30\tau^{PRS}(\phi = 0.6)$). For the stoichiometry flame, reaction R5 is not anymore the limiting reaction of the OHS submechanism presented in Table 2 and $TiCl_4$ is quasi-instantaneously converted into TiO_2 once the H_2O concentration is not negligible. In this case, TiO_2 production time is even smaller than the characteristic flame time ($\tau^{OHS}_{TiO_2}(\phi = 1.0) \approx 0.13\tau(\phi = 1.0)$) and $TiCl_4$ is completely converted into TiO_2 before the reaction is completed due to the presence of H_2O into the preheat zone. For both equivalence ratios, the first reactions in the OHS submechanism are faster than the first reactions of the DOS submechanism so that hydrolysis is always the main conversion process when using the OHS model ($\tau^{DOS}_{TiCl_4} > \tau^{OHS}_{TiCl_4}$) . Compared to the DOS model, accounting for $TiCl_4$ hydrolysis in the OHS scheme allows to predict a fast production of TiO_2 nanoparticles close to the flame front as expected in experiments. This observation confirms that hydrolysis is likely to be the dominant process leading to titanium dioxide particle formation in premixed flames.

A further comparison of model predictions is performed by calculating solid particle volume fraction f_v, number density N_p and mean particle diameter assuming a monodisperse distribution $d_{moy} = \sqrt[3]{6\pi^{-1} f_v N_p^{-1}}$. These quantities are displayed in Fig. 8 for both equivalence ratios with the 3 submechanisms.

For the lean flame, the OHS model initially predicts a higher particle volume fraction (x$\leq$ 2 mm, Fig. 8a), but its growth rapidly drops down compared to the phenomenological model. As expected from

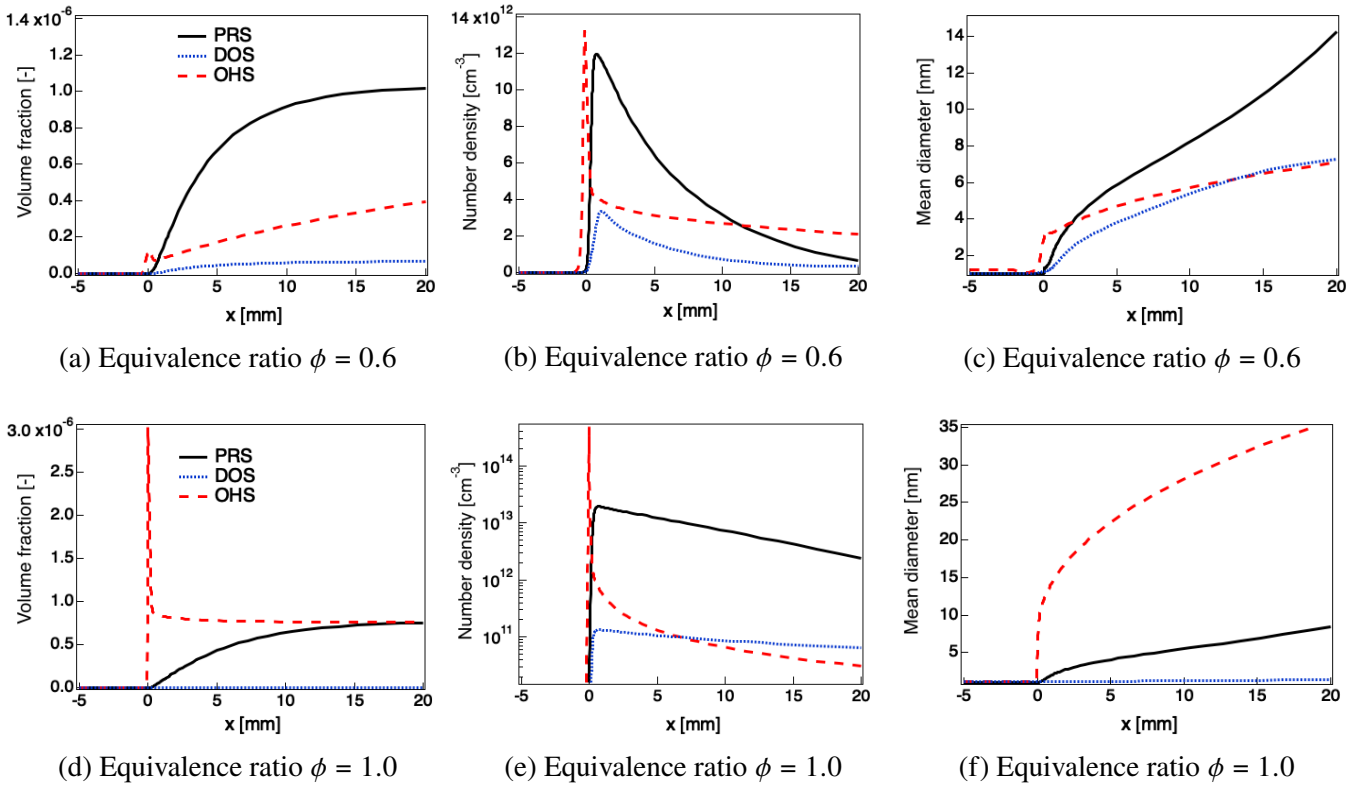

(a) Equivalence ratio $\phi = 0.6$ (b) Equivalence ratio $\phi = 0.6$ (c) Equivalence ratio $\phi = 0.6$

(d) Equivalence ratio $\phi = 1.0$ (e) Equivalence ratio $\phi = 1.0$ (f) Equivalence ratio $\phi = 1.0$

Figure 8 – Results for volume fraction, number density and mean diameter of TiO_2 using the PRS, the DOS and the OHS mechanisms are presented in black continuous, blue dotted and red dashed lines, respectively. 1-D premixed $CH_4/O_2/N_2$ flame. Same conditions as in Fig. 6.

the previous analysis, a low particle volume fraction production is predicted by the oxidation model. Results in terms of number density and mean diameter are qualitatively similar between the three models. For the stoichiometric flame, the PRS and OHS models predict similar conversion rates, i.e. the predicted volume fractions coincide in the final state in Fig. 8d. However, the $TiCl_4$ conversion processes are not identical, leading to a different solid particles nucleation and consequently different spatial evolutions of the number density (plotted in log scale in Fig. 8e) and mean diameter (Fig. 8f). This is due to the fact that small concentrations of H_2O diffusing in the flame preheat zone are sufficient to activate the hydrolysis reactions in the OHS scheme and that, once activated, these reactions are extremely fast. The global reaction of the PRS model is also activated in the preheat zone but it is characterized by a longer time so that a significant amount of nanoparticles is observed only downstream. As a consequence, a smaller number density N_p initially characterizes the TiO_2 production with the PRS model in Fig. 8e compared to the OHS model. Similarly, a fast production of volume fraction in a low-temperature region is observed leading to an initial high peak of f_v with the OHS model (Fig. 8d). This difference in $TiCl_4$ conversion rate leads to larger particle diameters in the OHS model predictions (Fig. 8f) compared to the PRS scheme. The DOS model predicts an almost negligible production of TiO_2 nuclei for $\phi = 1.0$ so that an extremely low number density and mean diameter are obtained with this model.

Particle size distributions (PSD) are plotted in Fig. 9 for the three submechanisms and the two equivalence ratios. For $\phi = 0.6$, close to the flame front ($x = 0.2$ mm), the PSD calculated with the DOS model features a lower first peak for small diameters than the one obtained with the two other schemes. When using the OHS model, the PSD shows the presence of bigger particles close to the flame front. Further downstream, the three models feature a similar PSD shape that tends toward a log-normal distribution, as expected from the experimental trends. Once a log-normal distribution is obtained, the aggregate size

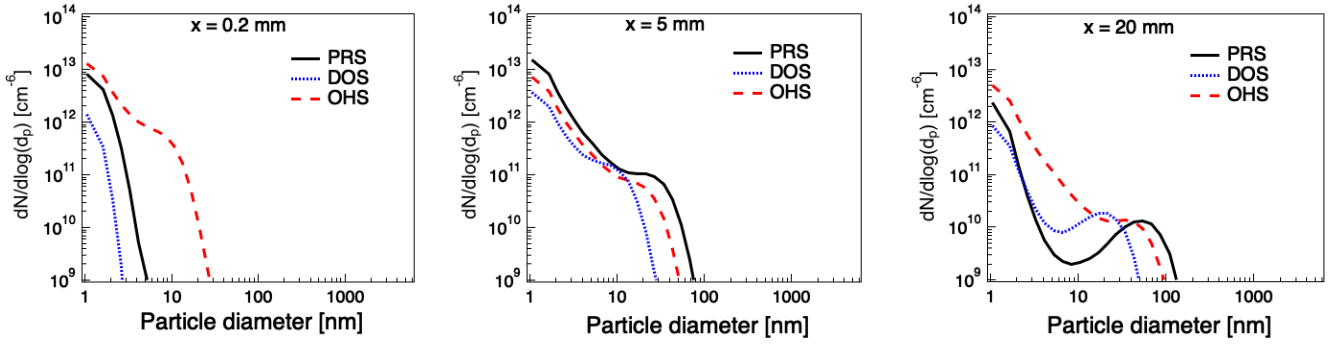

(a) x=0.2 mm, ϕ = 0.6 (b) x=5.0 mm, ϕ = 0.6 (c) x=20 mm, ϕ = 0.6

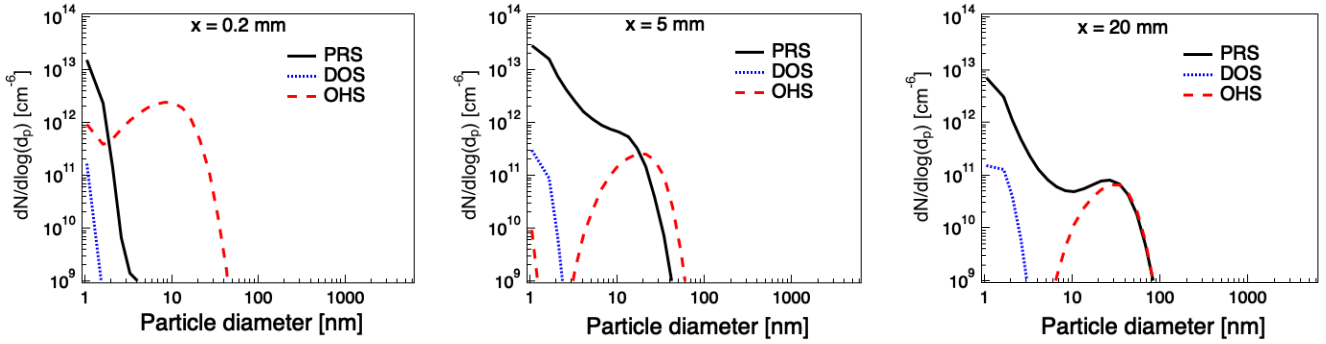

(d) x=0.2 mm, ϕ = 1.0 (e) x=5.0 mm, ϕ = 1.0 (f) x=20 mm, ϕ = 1.0

Figure 9 – Particle Size Distribution (PSD) for three axial positions in the premixed flame – same conditions as in Fig. 6 – for the three mechanisms: PRS (black continous), DOS (blue dotted), and OHS (red dashed) models.

predicted by the OHS model is slightly higher than the one predicted by the DOS model. This seems to indicate a similar effect of water vapor presence on aggregate size to what has been found in furnace reactors experiments [21]. For the stoichiometric flame, the DOS kinetics significantly underestimates the TiO_2 production rate compared to the PRS and OHS models, as already discussed, so that a one-peak distribution is observed with this model all along the flame. In contrast, the OHS and the PRS models lead to comparable TiO_2 volume fractions and both predict the fast production of big particles. The OHS kinetics is much faster than the PRS model so that the nucleation is completed even before reaching the flame front. Therefore, a sharp transition from the monodisperse distribution, characteristic of pure nucleation, to a log-normal distribution is observed when using the OHS model (x = 5 mm and x = 10 mm). In contrast, the PSD from the PRS model covers a large range of particle diameters, meaning that both nucleation and coagulation occur simultaneously in the reaction zone ($0 < x < 0.4$ mm) and in the postflame zone ($x > 0.4$ mm). However, the distributions corresponding to the large particle sizes are quite similar for the PRS and OHS models in terms of localization, level, and variance starting at distances exceeding x = 10 mm.

Differences in models predictions may be exhibited by examining the conversion yield η defined as the ratio of the molar flux of TiO_2 leaving the domain over the inlet molar flux of $TiCl_4$:

$$\eta = \frac{\text{Outlet } TiO_2}{\text{Inlet } TiCl_4} = \frac{\rho^{out} v^{out} W_{TiO_2} \overline{W}^{in} X^{out}_{TiO_2}}{\rho^{in} v^{in} W_{TiCl_4} \overline{W}_{out} X^{in}_{TiCl_4}} = \frac{\rho_s}{\rho^{out}} \frac{\overline{W}^{in}}{W_{TiCl_4}} \frac{f^{out}_v}{X^{in}_{TiCl_4}}, \tag{3.4}$$

where the superscripts "in" and "out" refer to the inlet and outlet conditions, respectively, and knowing $\rho^{in} v^{in} = \rho^{out} v^{out}$. An excessively long domain of L =10 m has been considered to calculate η. The conversion yield is calculated for different premixed flame equivalence ratios $\phi = \{0.6, 0.8, 1.0, 1.2, 1.4, 1.6\}$ for the

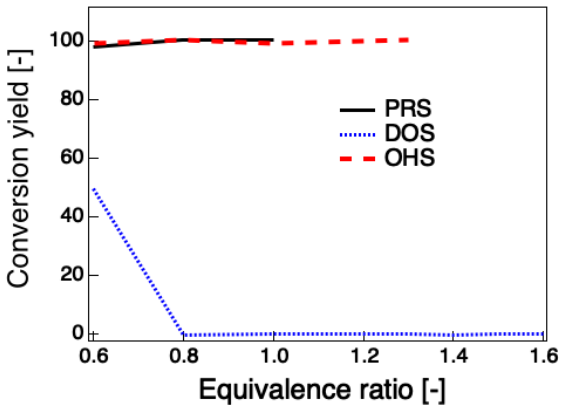

Figure 10 – Conversion yield η as a function of the equivalence ratio ϕ in the premixed flame for the three descriptions: PRS model, DOS kinetics, and OHS kinetics.

three $TiCl_4$ conversion mechanisms. As the rate constant of the PRS model is of order 0 in O_2, this model is not adapted to the simulation of rich flames as it may yield negative O_2 mass fractions. Therefore, the performances of the phenomenological model have only been tested under lean conditions. Results for the conversion yield are plotted in Fig. 10. For all considered equivalence ratios, the PRS and the OHS kinetics models lead to nearly 100 % conversion. For both schemes, the conversion yield is thus nearly independent of ϕ. Conversely, the DOS kinetics does not predict a fast conversion of $TiCl_4$ into TiO_2. The corresponding conversion yield is significant only for equivalence ratio $\phi = 0.6$, i.e. high O_2 concentration, and is negligible for higher equivalence ratios. The addition of the hydrolysis reactions to the detailed oxidation kinetics therefore appears as mandatory to reproduce the expected fast conversion rate for all equivalence ratios.

In general, the PRS model predicts a TiO_2 production that has a low dependency with respect to the equivalence ratio. On the contrary, the spatial evolution of TiO_2 production predicted with the DOS or the OHS models strongly depend on the flame operating conditions. As expected, when using the DOS mechanism a significant conversion is observed only for high O_2 concentration, i.e. under lean conditions. On the contrary, the OHS mechanism predicts a faster conversion for richer flames, characterized by high H_2O concentration. However, results with the OHS model far downstream from the flame front in terms of conversion rate and PSD are similar to predictions with the PRS model that by construction is expected to represent the global experimental trends in terms of final TiO_2 production with no guarantee of a correct description of the chemical pathways and correspondingly of the spatial evolutions of Ti-containing species.

3.3 1-D counterflow flames

The behaviour of the three conversion submechanisms is now investigated in counterflow flames, schematically presented in Fig. 11, in a configuration where pure CH_4 is injected on the right side against pure O_2 injected from the left side at a temperature $T = 500$ K and pressure $p = 1$ atm. The strain rate is α =100 s^{-1}. Gaseous $TiCl_4$ is injected with a mass fraction $Y^{inj}_{TiCl_4}$=5%. Two cases are considered: $TiCl_4$ is injected either at the fuel side or at the oxidizer side. Pure O_2 has been considered instead of air to evaluate the contribution of oxidation pathways for its most favourable conditions corresponding to the injection of $TiCl_4$ on the oxidizer side. An axisymmetric configuration is considered and a 1-D formulation along the central axis in used [51].

The flame structure obtained for the fuel-side case with the OHS submechanism is presented in Fig. 12. The stagnation plane is located at $x = 0$ mm. When considering the oxidizer-side case with the two other submechanisms, only small differences in terms of temperature and major species concentrations are

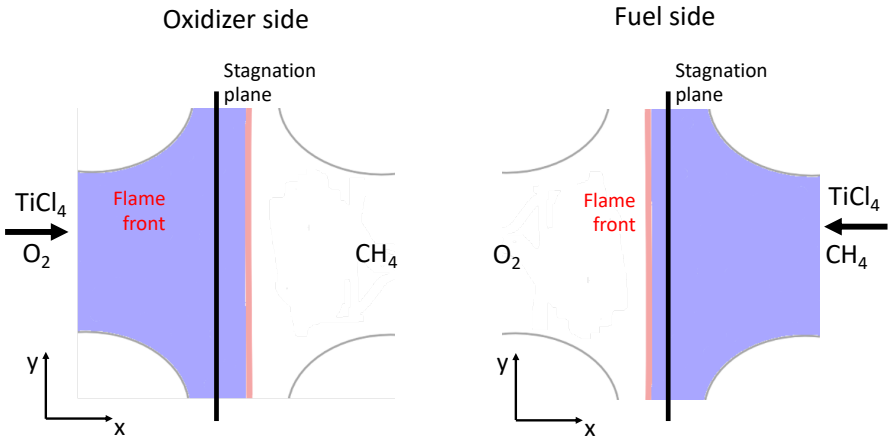

Figure 11 – Schematic of 1-D counterflow flame configuration. Left: $TiCl_4$ is injected at the oxidizer side. Right: $TiCl_4$ is injected at the fuel side.

detected (not shown), indicating that the $TiCl_4$ chemistry does not greatly modify the methane oxidation process in this configuration as in the laminar premixed flames analyzed previoulsy.

The profiles of $TiCl_4$ and $TiO_{2(s)}$ mass fractions for both fuel-side and oxidizer-side injections are plotted in Fig. 13. To interpret the results, it is important to remember that $TiO_{2(s)}$ profiles result of convection, thermophoresis and chemical processes:

- Solid particles are mainly produced on the side where $TiCl_4$ is injected once temperature or/and H_2O concentration are sufficiently high. The TiO_2 production region, i.e. where the TiO_2 production rate is higher than 1% of its maximum value, is identified by vertical blue lines. When $TiCl_4$ is injected on the oxidizer side, the TiO_2 production region is found on the injection side ($x < 0$ mm) for all three submechanisms, even if its extension and position depend on the submechanism. When $TiCl_4$ is injected on the fuel side, the nucleation zone covers both sides when using the PRS or the DOS models, while it arises in a small zone in the injection side with the OHS model. For both injection sides, the oxidation model leads to a negligible production of TiO_2. As a result of the nucleation process, a local maximum of TiO_2 mass fraction is found in the injection zone for all considered cases.

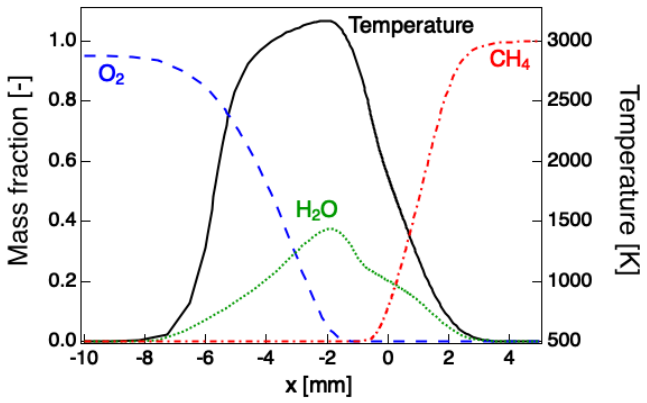

Figure 12 – 1-D non-premixed counterflow diffusion CH_4/O_2 flame. The strain rate is $100\,s^{-1}$. The flame stagnation plane is located at $x = 0$ mm.

- Once produced, solid particles are convected towards the stagnation plane, located at $x = 0$ mm. Particles are expected not to cross this plane, so that a maximum of TiO_2 concentration is expected to form near that plane. However, solid particles are also subjected to thermophoretical diffusion, transporting nanoparticles towards lower temperature region. The position of temperature maximum value is marked by the red vertical line. Convection and thermophoresis processes occur simultaneously and can have a similar or an opposite effect on the profile of TiO_2 mole concentration depending on the zone, eventually leading to the presence of additional local maxima.

Since particle evolution strongly depends on the localization of their nucleation region relatively to the stagnation plane and the position of the maximum temperature, $TiO_{2(s)}$ profiles notably differ depending on the $TiCl_4$ injection side and the retained chemical description.

In analogy with the performances obtained on the premixed flames, a fast consumption of $TiCl_4$ is observed with the PRS and the DOS models and an even faster $TiCl_4$ consumption is found when using the OHS submechanism, independently of the injection side. In both cases, the PRS and OHS models predict a significantly higher conversion rate of $TiCl_4$ into TiO_2 than the DOS model, which predicts a fast $TiOCl_2$ production but a nearly negligible conversion into TiO_2. With the OHS kinetics, $TiCl_4$ is rapidly consumed and is essentially converted into TiO_2 for both injection cases, following the hydrolysis pathways. Significant differences can be observed between the OHS mechanism and the PRS model. First, in both configurations, a higher mass fraction is obtained when using the OHS model than the PRS results. Second, the $TiCl_4$ conversion process occurs upstream when using the OHS model, so that the $TiO_{2(s)}$ production is not localized in the same region. For all submechanisms, the injection of $TiCl_4$ with the oxidizer represents the most efficient way to produce TiO_2 nanoparticles.

Results on the solid phase in terms of particle volume fraction, number density and mean particle diameter obtained with the three submechanisms are compared in Fig. 14. Results with the DOS scheme are not reported for the fuel side case since it predicts a negligible TiO_2 production, whereas an extremely low, yet non-zero, production is obtained for the most favorable case, i.e. injection in the oxidizer side.

When $TiCl_4$ is injected from the oxidizer side, the three submechanisms present a qualitatively similar production of TiO_2 nanoparticles, but the DOS model predicts an extremely low production. One distinguishing feature of the OHS model is that the first particles are formed upstream so that the TiO_2 volume fraction and number density profiles exhibit a local maximum before reaching the high temperature region ($x \approx 7$ mm, Figs. 14a and b). Differences between the three models are more pronounced when $TiCl_4$ is injected on the fuel-side, with changes in the position of the region where TiO_2 is formed. More specifically, production of TiO_2 is extremely fast when using the OHS model so that nucleation is completed in the injection side. On the contrary, $TiCl_4$ consumption with the PRS model is not ended before the stagnation plane so that TiO_2 nucleation occurs on both sides of this plane. As a consequence, the number density and mean diameter profiles are quite different when using the PRS or the OHS models.

Similarly, the PSD evolution in the flame presented in Fig. 15 strongly depends on the chemical scheme. As in the premixed case, the OHS kinetics is faster than the PRS model, itself faster than the DOS model. As a consequence, the transition towards a log-normal PSD is much faster with the OHS scheme than with the other schemes. The PRS model and OHS scheme yield similar PSDs for particle diameters greater than 30 nm for injection in the oxidizer-side (x=0 mm, top), indicating that the OHS model predicts a final production coherent with the PRS model while providing additional information on the chemical pathways, i.e. on the spatial evolution of TiO_2 production in the flame vicinity.

It is interesting to determine the conversion yield η of Ti Cl_4. To do so, let us consider that $TiCl_4$ is injected from the left (here the oxidizer side) into the control volume defined by red lines in Fig. 16 spreading from $x = X^{inj}$ to $x = +\infty$ over a height of $y = H$. The conversion yield is then defined as the ratio of the molar flux of TiO_2 leaving the flame domain over the molar flux of $TiCl_4$ injected into the control volume. In order to avoid that a part of fresh $TiCl_4$ leaves the control volume without being converted, X^{inj} should be located close to the flame front. This point is defined here as the axial position where the temperature starts increasing, namely: $(T(X^{inj}) - T^{-\infty})/(T^{max} - T^{-\infty}) \geq 10^{-3}$.

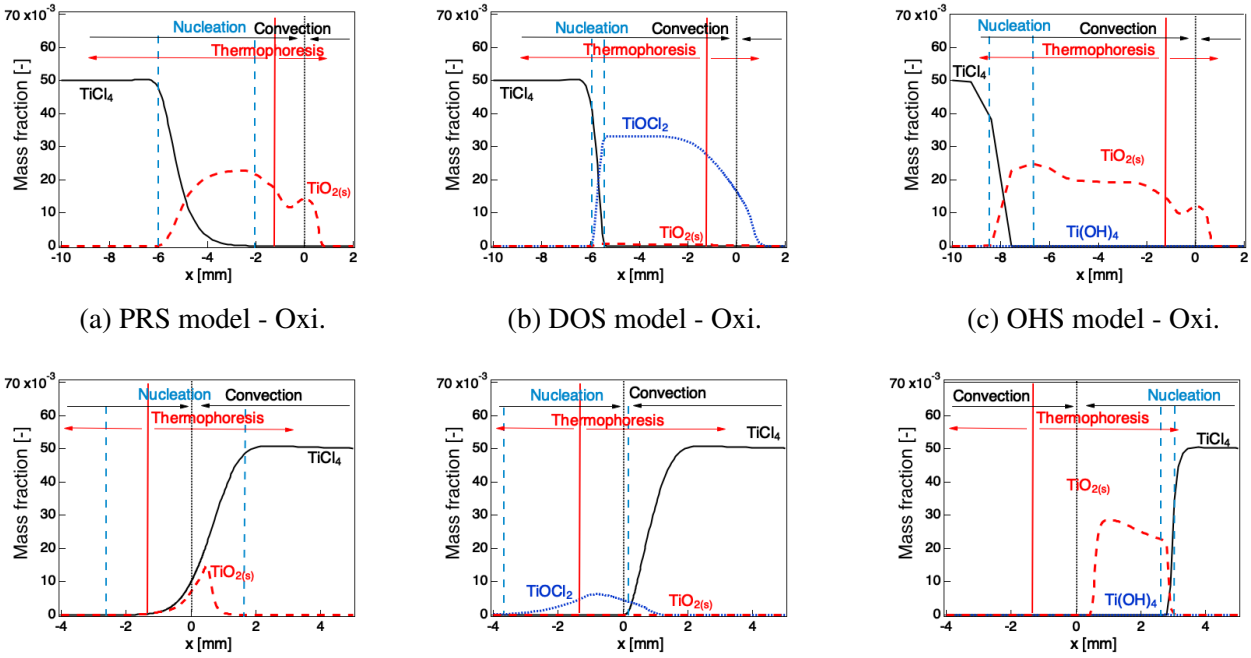

(a) PRS model - Oxi. (b) DOS model - Oxi. (c) OHS model - Oxi.

(d) PRS model - Fuel (e) DOS model - Fuel (f) OHS model - Fuel

Figure 13 – 1-D non-premixed counterflow CH_4/O_2 flame using PRS, DOS and OHS models. The strain rate is $100\,s^{-1}$ and the $TiCl_4$ is injected on the oxidizer (top) or fuel (bottom) sides with a mass fraction of 5 %. The flame stagnation plane is located at $x = 0$ mm. Vertical dotted grey lines indicate the TiO_2 production zone. Same conditions as in Fig. 12.

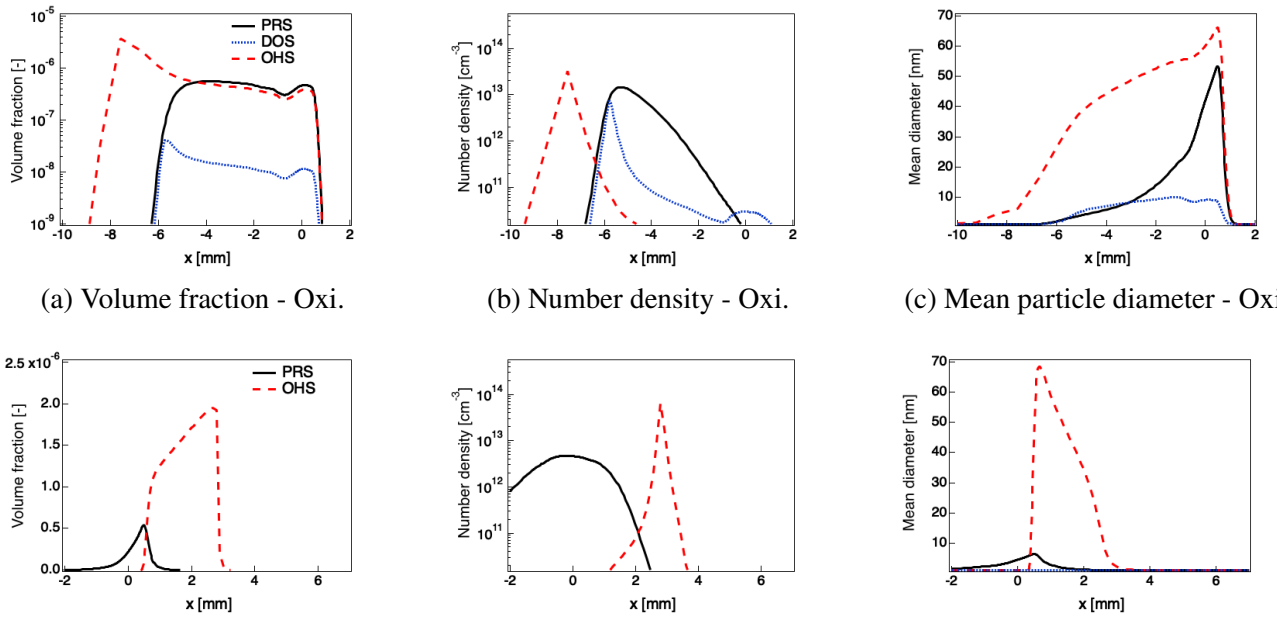

(a) Volume fraction - Oxi. (b) Number density - Oxi. (c) Mean particle diameter - Oxi.

(d) Volume fraction - Fuel (e) Number density - Fuel (f) Mean particle diameter - Fuel

Figure 14 – Results for volume fraction, number density and mean particle diameter using the PRS and the OHS mechanisms represented in red dashed and black continuous lines, respectively. 1-D counterflow CH_4/O_2 flame with $TiCl_4$ injection on the oxidizer (top) and fuel (bottom) sides. Results with the DOS scheme are reported in dotted blue lines only for the oxidizer side. Same conditions as in Fig. 12.

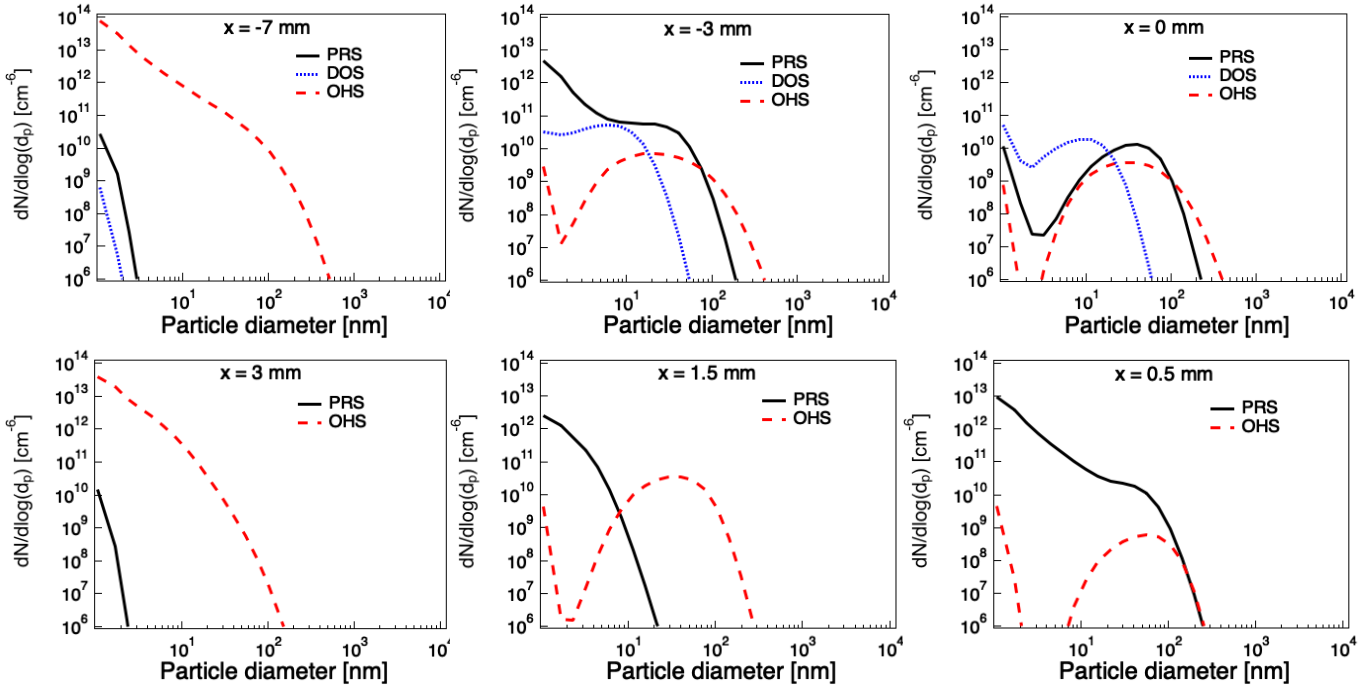

Figure 15 – Particle Size Distribution (PSD) for three axial positions in the counterflow flame for the three mechanisms: PRS, DOS and OHS models. 1-D counterflow CH_4/O_2 flame with $TiCl_4$ injection on the oxidizer (top) and fuel (bottom) sides.

In these conditions, the conversion yield η reads:

$$\eta = \frac{\int_{X^{inj}}^{+\infty} n_{TiO_2}(x)\, u(x,H)\; dx}{\int_0^H n_{TiCl_4}(X^{inj})\, v(X^{inj})\; dy}. \tag{3.5}$$

where n_k (cm^{-3}) is the number density of the k^{th} species. As in the 1-D formulation we have $u(x,H) = H\,U(x)$, one obtains:

$$\eta = \frac{\int_{X^{inj}}^{+\infty} n_{TiO_2}(x)\, U(x)\; dx}{n_{TiCl_4}(X^{inj})\, v(X^{inj})}. \tag{3.6}$$

It should be noted that the conversion yield does not depend on H.

The conversion yield is plotted in Fig. 17 as a function of the strain rate α for the three schemes considered. For all schemes, the conversion rate is a decreasing function of the strain rate, as increasing the strain rate lowers the residence time in the flame. For all strain rates, the OHS scheme leads to a higher conversion yield than the PRS model, itself leading to a much higher rate than the DOS scheme. As in the premixed flame, the detailed oxidation DOS model does not predict a fast conversion of $TiCl_4$ into TiO_2, in contrast with experimental results in diffusion flames [18, 43]. Compared to the premixed flame, none of the proposed kinetics predict full conversion in the counterflow configuration. The phenomenological PRS model, which is known to be fast, predicts lower conversion yields than the OHS scheme including hydrolysis, with ranges below 40 % at 600 s^{-1}. This is likely because the OHS scheme is extremely fast and it is less sensitive to the residence time in the flame. Adding the hydrolysis mechanism allows to recover the experimental trend concerning final products, fast conversion of $TiCl_4$ into TiO_2 and evolution of the PSD towards a log-normal distribution of particle sizes.

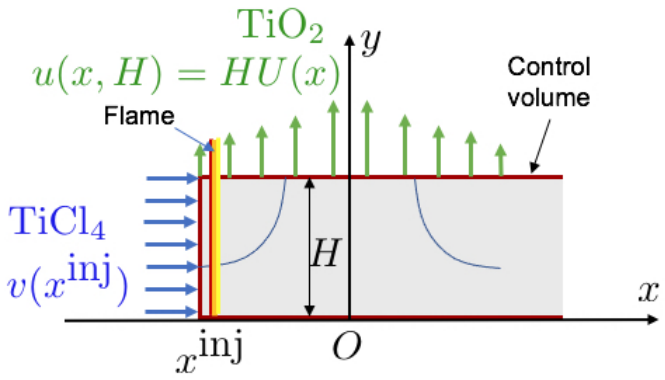

Figure 16 – Schematic representation of the control volume used to determine the conversion yield in the counterflow flame configuration. The control surface is drawn in dark red and the volume is shown in gray.

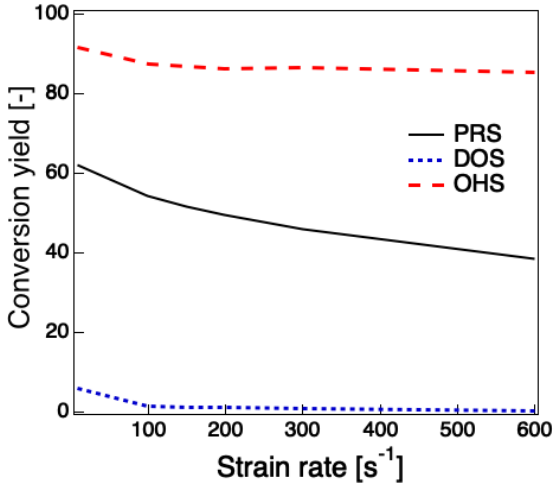

Figure 17 – Conversion yield η plotted as a function of the strain rate α in the counterflow flame when $TiCl_4$ is injected from the oxidizer side – same conditions as in Fig. 12 – for the three mechanisms: PRS, DOS and OHS.

3.4 Co-flow flame

Finally, the three models are evaluated in an axisymmetric co-flow methane/air flame, schematically represented in Fig. 18a, reproducing the experimental setup of Xu et al. [41]. A $TiCl_4/N_2$ mixture is injected via an inner tube with a volume fraction of $TiCl_4$=10%. It it conveyed by an injection of CH_4/Ar mixture, surrounded by an outer coflow of O_2 and an external coflow of N_2.

Compared to the original configuration, corresponding to a flame in the transitional laminar to turbulent regime, the mass flow rates have been halved to preserve a laminar flow. The operating conditions are gathered in Table 4.

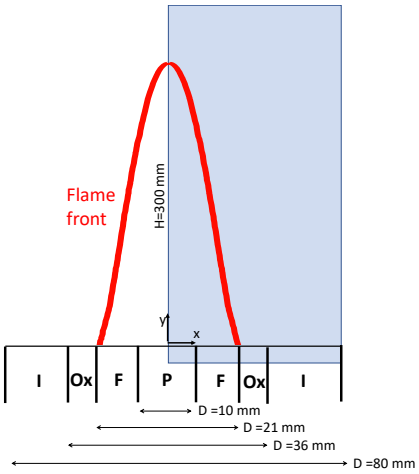

(a) Schematic of the 2-D co-flow flame.

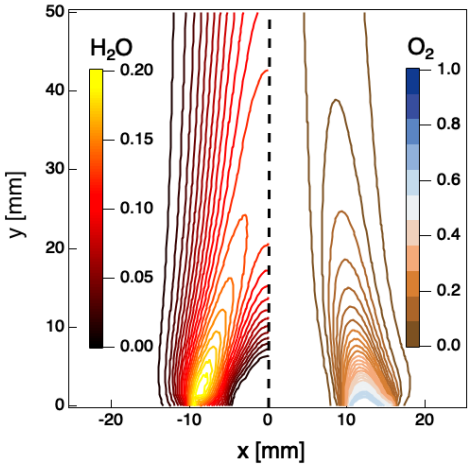

(b) O_2 and H_2O mass fraction fields from the OHS are displayed to identify the oxidation and hydrolysis zones.

Figure 18 – 2-D co-flow flame configuration.

Inlet	Temperature	Mass fraction Y_k	Velocity	Inner diameter (wall thickness)
Precursor (P)	500 K	$TiCl_4$:0.429 / N_2:0.571	0.11 m/s	10 (0.5) mm
Pilot flame (F)	500 K	CH_4:0.448 / Ar:0.552	0.085 m/s	21 (0.75) mm
Oxidizer (Ox)	500 K	O_2:1.0	0.052 m/s	36 (1) mm
Inert (I)	500 K	N_2:1.0	0.05 m/s	80 mm

Table 4 – Operating conditions for the 2-D co-flow flame.

The simulation is performed using the OpenFoam solver using the Tabulation of Dynamic Adaptive Chemistry (TDAC) model [52], coupling a tabulation method with a mechanism reduction method, and assuming an axisymmetric flow. The geometry reproduces the burner from 20 mm before the injection ($y = -20$ mm) up to $y = 300$ mm (blue square in Fig. 18a) and it extends radially up to $x = 80$ mm. The grid is composed of approximately 18000 cells presenting a spatial resolution of 0.4 mm in the region close to the burner outlet. For this configuration, only the gaseous phase is simulated and results for TiO_2 nanoparticles can be directly derived from gaseous TiO_2 mass fraction, since we have assumed that nucleation is an infinitely fast process. Numerical difficulties were encountered when using the phenomenological PRS model since $TiCl_4$ is injected together with N_2 so that the reaction rate of Eq. (2.4) can be non-zero even when O_2 is absent when the flame temperature is sufficiently high, possibly leading to negative O_2 mass fractions. To overcome this problem, the reaction rate for O_2 species coming from the phenomenological equation has been forced to zero. Even if O-atoms conservation is not guaranteed, the O_2 consumption is expected to be small and will not greatly affect the results.

Fields of O_2 and H_2O mass fractions obtained with the OHS model are shown in Fig. 18b and reveal regions where oxidation and hydrolysis of $TiCl_4$ may occur. The two species do not overlap everywhere so that oxidation and hydrolysis chemical pathways may play a different role in TiO_2 formation in the co-flow flame. A significant H_2O level is found along the flame centerline, where $TiCl_4$ is injected, while O_2 exists at a distance from the axis. Results for $TiCl_4$ and TiO_2 mass fractions for the three submechanisms are plotted in the top row of Fig. 19. To illustrate the different kinetics, the $TiCl_4$ consumption and TiO_2 production zones are marked in blue and red, respectively, in Figs. 19d-19f.

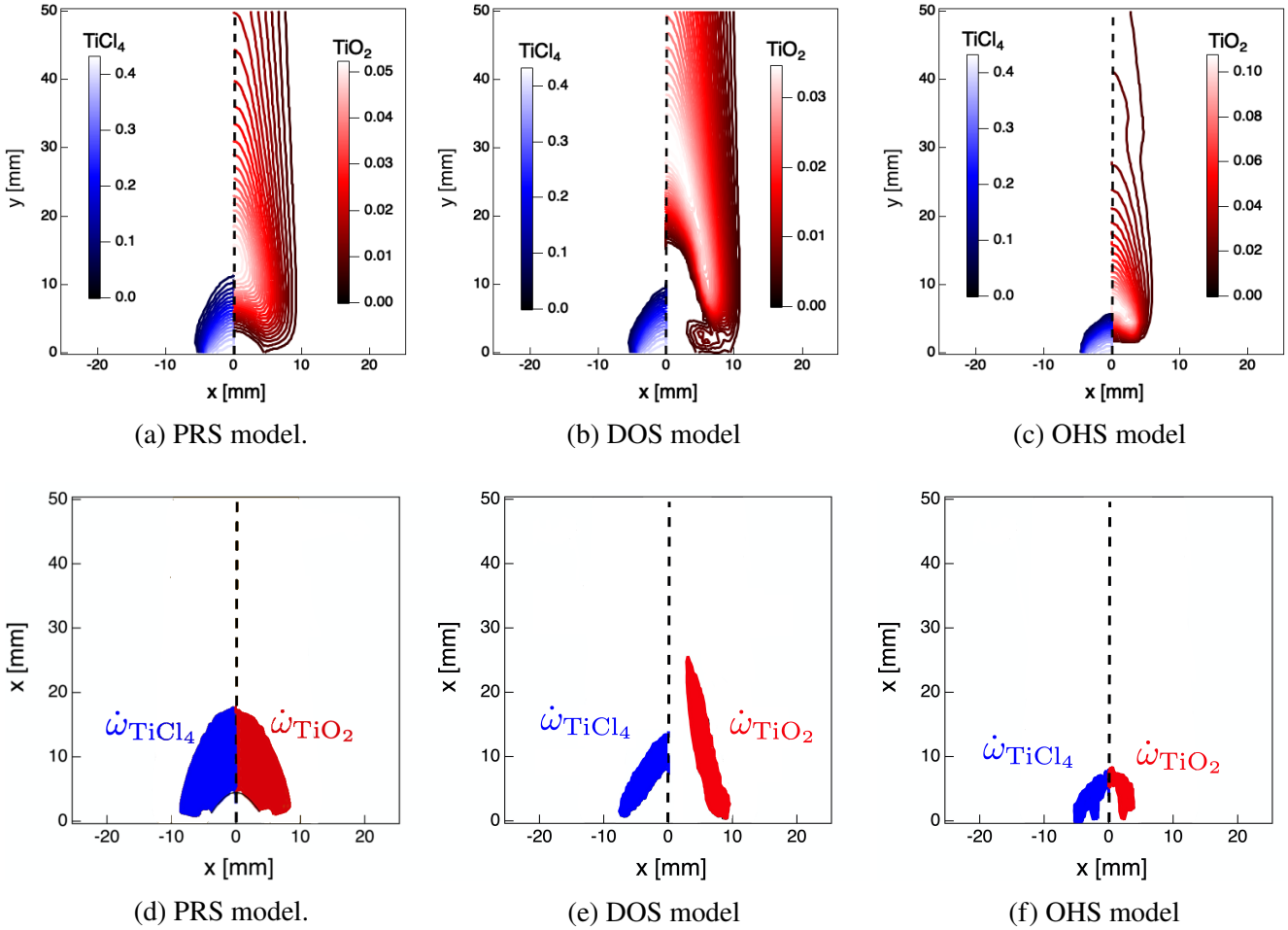

(a) PRS model. (b) DOS model (c) OHS model

(d) PRS model. (e) DOS model (f) OHS model

Figure 19 – Results for a 2-D co-flow flame using the PRS model, the DOS kinetics and the newly OHS mechanism. a-c) $TiCl_4$ and TiO_2 mass fractions. d-f) $TiCl_4$ consumption and TiO_2 production zones are identified in blue and red.

The locations of $TiCl_4$ consumption and TiO_2 production zones strongly depend on the retained kinetics. The phenomenological PRS and the oxidation DOS models predict similar evolutions of $TiCl_4$ concentration whereas $TiCl_4$ consumption is completed in a smaller region when using the OHS model indicating a faster reaction as previously observed for premixed and counterflow diffusion flames. The TiO_2 production zone lies near the centerline for the PRS and the OHS models, differing from the DOS model's results due to a very small O_2 concentration in this region (Fig. 18). As already deduced in 1-D configurations, the PRS and OHS models predict a fast conversion of $TiCl_4$ into TiO_2 so that $TiCl_4$ consumption and TiO_2 production zones almost overlap. On the contrary, these two processes do not occur in the same zone when considering the DOS model, indicating a fast consumption of $TiCl_4$ but a slow TiO_2 production. As a consequence, the maximum value of TiO_2 mass fraction and its location vary with the submechanism: a high yield is observed closer to the injection with the fastest OHS model, whereas a small yield of TiO_2 is predicted downstream with the DOS mechanism. This behaviour is in line with results presented for premixed and counterflow laminar flames: the oxidation mechanism activates when a sufficiently high concentration of O_2 is observed and predicts a slower TiO_2 production compared to the other two submechanisms. Overall, the hydrolysis pathway plays an important role when the H_2O concentration is high leading to an extremely fast and efficient conversion of $TiCl_4$.

4 Conclusion

The production of titanium dioxide nanoparticles by flame synthesis is numerically investigated in standard laminar flame configurations, by focusing on the role that $TiCl_4$ hydrolysis may play on TiO_2 flame synthesis. Three submechanisms for $TiCl_4$ conversion into TiO_2 are considered: a phenomenological PRS scheme that reproduces global experimental trends in terms of final products, a detailed DOS mechanism only accounting for $TiCl_4$ oxidation and a newly developed OHS mechanism describing both $TiCl_4$ oxidation and hydrolysis. The DOS kinetics developed in dry configurations is characterized by extremely long TiO_2 formation time scales in flames when O_2 concentration is low, leading to low conversion yields, in contrast with experimental data. On the contrary, the OHS scheme predicts for all considered cases a fast and efficient TiO_2 production leading to a final log-normal particle size distribution, as expected from experimental observations and state-of-the-art phenomenological results, while giving access to detailed chemical pathways. These results suggest that $TiCl_4$ hydrolysis is a major contributor to TiO_2 production in flames, due to the presence of water vapor and the high reactivity of $TiCl_4$ with vapor.

As a perspective, the proposed five-step model for $TiCl_4$ hydrolysis would need to be replaced by a more complex kinetic scheme including additional intermediate species and reactions to obtain an improved quantitative description of the process. A deeper validation and characterization of the hydrolysis chemical pathways in terms of reactions and kinetic parameters are sought. For this, it would be useful to develop experiments not only focused on final products but also providing information on the spatial evolution of Ti-species in the flame. Specifically, the location where TiO_2 is produced would provide information on whether hydrolysis or oxidation dominate the process by verifying if it occurs in a region where H_2O or O_2 are present. However, the proposed OHS kinetics represents a first step towards an accurate characterization of the combustion processes governing nanoparticles flame synthesis, essential for the optimization of industrial systems relying on this process.

Acknowledgments

The authors wish to thank the reviewers for their helpful comments. The support of the European Research Council (ERC) under the European Union Horizon 2020 research and innovation programme (grant agreement No. 757912) is gratefully acknowledged.

References

[1] G. A. Kelesidis, E. Goudeli, S. E. Pratsinis, Flame synthesis of functional nanostructured materials and devices: Surface growth and aggregation, Proc. Combust. Inst. 36 (2017) 29–50.

[2] C. Schulz, T. Dreier, M. Fikri, H. Wiggers, Gas-phase synthesis of functional nanomaterials: Challenges to kinetics, diagnostics, and process development, Proc. Combust. Inst. 37 (2019) 83–108.

[3] F. Meierhofer, U. Fritsching, Synthesis of metal oxide nanoparticles in flame sprays: review on process technology, modeling, and diagnostics, Energ. Fuel. 35 (2021) 5495 – 5537.

[4] N. A. Ramos-Delgado, M. Ã. Gracia-Pinilla, R. V. Mangalaraja, K. O'Shea, D. D. Dionysiou, Industrial synthesis and characterization of nanophotocatalysts materials: titania, Nanotechnol. Rev. 5 (2016) 467–479.

[5] G. Kelesidis, S. Pratsinis, A perspective on gas-phase synthesis of nano materials: process design, impact and outlook, Chem. Eng. J. 421 (2021) 129884.

[6] M. J. Gazquez, J. P. Bolivar, R. Garcia-Tenorio, F. Vaca, A review of the production cycle of titanium dioxide pigment, Mater. Sci. Appl. 5 (2014) 441–458.

[7] P. George, Formation of Ti02 Aerosol from the Combustion Supported Reaction of TiCl4 and O2, Faraday Symp. Chem. S. 7 (1973) 63–71.

[8] J. Han, H. Chang, J. Lee, H. Chang, The Aggregation of Thermally Stable Particles in a Premixed Flat Flame Aerosol Reactor, Aerosol Sci. Tech. 37 (2003) 550–564.

[9] C.-H. Hung, J. L. Katz, Formation of mixed oxide powders in flames: Part I. TiO2-SiO2, J. Mater. Res. 7 (1992) 1861–1869.

[10] J. Hyeon-Lee, G. Beaucage, S. E. Pratsinis, S. Vemury, Fractal Analysis of Flame-Synthesized Nanostructured Silica and Titania Powders Using Small-Angle X-ray Scattering, Langmuir 14 (1998) 5751–5756.

[11] H. D. Jang, J. Jeong, The Effects of Temperature on Particle Size in the Gas-Phase Production of TiO $_2$, Aerosol Sci. Tech. 23 (1995) 553–560.

[12] A. Kobata, K. Kusakabe, S. Morooka, Growth and transformation of TiO2 crystallites in aerosol reactor, AIChE J. 37 (1991) 347–359.

[13] S. E. Pratsinis, W. Zhu, S. Vemury, The role of gas mixing in flame synthesis of titania powders, Powder Technol. 86 (1996) 87–93.

[14] S. E. Pratsinis, H. Bai, P. Biswas, M. Frenklach, S. V. R. Mastrangelo, Kinetics of Titanium(IV) Chloride Oxidation, J. Am. Ceram. Soc. 73 (1990) 2158–2162.

[15] K. Nakaso, T. Fujimoto, T. Seto, M. Shimada, K. Okuyama, M. M. Lunden, Size Distribution Change of Titania Nano-Particle Agglomerates Generated by Gas Phase Reaction, Agglomeration, and Sintering, Aerosol Sci. Tech. 35 (2001) 929–947.

[16] M. K. Akhtar, Y. Xiong, S. E. Pratsinis, Vapor synthesis of titania powder by titanium tetrachloride oxidation, AIChE J. 37 (1991) 1561–1570.

[17] Y. Xiong, M. Kamal Akhtar, S. E. Pratsinis, Formation of agglomerate particles by coagulation and sinteringâ Part II. The evolution of the morphology of aerosol-made titania, silica and silica-doped titania powders, J. Aerosol Sci. 24 (1993) 301–313.

[18] L.-D. Chen, W. Roquemore, Visualization of jet flames, Combust. Flame 66 (1) (1986) 81–86.

[19] W. M. Roquemore, R. S. Tankin, H. H. Chiu, S. A. Lottes, A study of a bluff-body combustor using laser sheet lighting, Exp. Fluids 4 (1986) 205–213.

[20] M. C. Heine, S. E. Pratsinis, Agglomerate TiO2 Aerosol Dynamics at High Concentrations, Part. Part. Syst. Char. 24 (2007) 56–65.

[21] M. K. Akhtar, S. Vemury, S. E. Pratsinis, Competition between TiCl4 hydrolysis and oxidation and its effect on product TiO2 powder, AIChE J. 40 (1994) 1183–1192.

[22] T. S. Totton, R. Shirley, M. Kraft, First-principles thermochemistry for the combustion of TiCl4 in a methane flame, Proc. Combust. Inst. 33 (2011) 493–500.

[23] R. H. West, M. S. Celnik, O. R. Inderwildi, M. Kraft, G. J. O. Beran, W. H. Green, Toward a Comprehensive Model of the Synthesis of TiO_2 Particles from $TiCl_4$, Ind. Eng. Chem. Res. 46 (2007) 6147–6156.

[24] R. H. West, R. A. Shirley, M. Kraft, C. F. Goldsmith, W. H. Green, A detailed kinetic model for combustion synthesis of titania from TiCl4, Combust. Flame 156 (2009) 1764–1770.

[25] M. Mehta, Y. Sung, V. Raman, R. O. Fox, Multiscale Modeling of TiO2 Nanoparticle Production in Flame Reactors: Effect of Chemical Mechanism, Ind. Eng. Chem. Res. 49 (2010) 10663–10673.

[26] M. Mehta, V. Raman, R. O. Fox, On the role of gas-phase and surface chemistry in the production of titania nanoparticles in turbulent flames, Chem. Eng. Sci. 104 (2013) 1003–1018.

[27] C. S. Lindberg, M. Y. Manuputty, J. Akroyd, M. Kraft, A two-step simulation methodology for modelling stagnation flame synthesised aggregate nanoparticles, Combust. Flame 202 (2019) 143–153.

[28] J. Wei, A. Ostadhossein, S. Li, M. Ihme, Kinetics for the hydrolysis of Ti(OC3H7)4: A molecular dynamics simulation study, Proc. Combust. Inst. 38 (2021) 1433–1440.

[29] M. Mehta, R. O. Fox, P. Pepiot, Reduced Chemical Kinetics for the Modeling of TiO2 Nanoparticle Synthesis in Flame Reactors, Ind. Eng. Chem. Res. 54 (2015) 5407–5415.

[30] S. E. Pratsinis, P. T. Spicer, Competition between gas phase and surface oxidation of TiCl4 during synthesis of TiO2 particles, Chem. Eng. Sci. 53 (1998) 1861–1868.

[31] P. Rodrigues, Modélisation multiphysique de flammes turbulentes suitées avec la prise en compte des transferts radiatifs et des transferts de chaleur pariétaux., Ph.D. thesis, Université Paris-Saclay (2018).

[32] J.-M. Orlac'h, N. Darabiha, V. Giovangigli, B. Franzelli, Importance of mass and enthalpy conservation in the modelling of titania nanoparticles flame synthesis, Combust. Theory Model. 25 (2021), 389–412.

[33] L. Waldmann, K. Schmitt, Thermophoresis and diffusiophoresis of aerosols, in: Aerosol Science, davies, c. n. Edition, Academic Press, New York, 1966, pp. 137–162.

[34] B. V. Derjaguin, A. I. Storozhilova, Y. I. Rabinovich, Experimental verification of the theory of thermophoresis of aerosol particles, J. Colloid Interf. Sci. 21 (1966) 35–58.

[35] W. Sutherland, The viscosity of gases and molecular force, The London, Edinburgh, and Dublin Philosophical Magazine and Journal of Science 223 (1893) 507–531.

[36] S. E. Pratsinis, Simultaneous nucleation, condensation, and coagulation in aerosol reactors, J. Colloid Interf. Sci. 124 (1988) 416–427.

[37] R. N. Ghoshtagore, Mechanism of Heterogeneous Deposition of Thin Film Rutile, J. Electrochem. Soc. 117 (1970) 529.

[38] P. T. Spicer, O. Chaoul, S. Tsantilis, S. E. Pratsinis, Titania formation by TiCl4 gas phase oxidation, surface growth and coagulation, J. Aerosol Sci. 33 (2002) 17–34.

[39] S. Tsantilis, S. E. Pratsinis, Narrowing the size distribution of aerosol-made titania by surface growth and coagulation, J. Aerosol Sci. 35 (2004) 405–420.

[40] N. Morgan, C. Wells, M. Goodson, M. Kraft, W. Wagner, A new numerical approach for the simulation of the growth of inorganic nanoparticles, J. Comput. Phys. 211 (2006) 638–658.

[41] Z. Xu, H. Zhao, H. Zhao, CFD-population balance Monte Carlo simulation and numerical optimization for flame synthesis of TiO2 nanoparticles, Proc. Combust. Inst. 36 (2017) 1099–1108.

[42] M. Rigo, P. Canu, L. Angelin, G. Della Valle, Kinetics of TiCl4 Hydrolysis in a Moist Atmosphere, Ind. Eng. Chem. Res. 37 (1998) 1189–1195.

[43] W. Zhu, S. E. Pratsinis, Flame Synthesis of Nanosize Powders: Effect of Flame Configuration and Oxidant Composition, in: G.-M. Chow, K. E. Gonsalves (Eds.), Nanotechnology, Vol. 622 of ACS Symposium Series, Abstr. Pap. Am. Chem S. (1996) 64–78.

[44] S. K. Friedlander, C. S. Wang, The Self-Preserving Particle Size Distribution for Coagulation by Brownian Motion ~, J. Colloid Interf. Sci. 22 (1966) 7.

[45] S. Vemury, K. A. Kusters, S. E. Pratsinis, Time-lag for attainment of the self-preserving particle size distribution by coagulation, J. Colloid Interf. Sci. 165 (1994) 56–59.

[46] J. Akroyd, A. J. Smith, R. Shirley, L. R. McGlashan, M. Kraft, A coupled CFD-population balance approach for nanoparticle synthesis in turbulent reacting flows, Chem. Eng. Sci. 66 (2011) 3792–3805.

[47] A. Boje, J. Akroyd, S. Sutcliffe, J. Edwards, M. Kraft, Detailed population balance modelling of TiO2 synthesis in an industrial reactor, Chem. Eng. Sci. 164 (2017) 219–231.

[48] C. Lindberg, J. Akroyd, M. Kraft, Developing breakage models relating morphological data to the milling behaviour of flame synthesised titania particles, Chem. Eng. Sci. 166 (2017) 53–65.

[49] T.-H. Wang, A. M. Navarrete-Lopez, S. Li, D. A. Dixon, J. L. Gole, Hydrolysis of TiCl4: Initial Steps in the Production of TiO2, J. Phys. Chem. A 114 (2010) 7561–7570.

[50] C. S. Lindberg, M. Y. Manuputty, P. Buerger, J. Akroyd, M. Kraft, Numerical simulation and parametric sensitivity study of titanium dioxide particles synthesised in a stagnation flame, J. Aerosol Sci. 138 (2019) 105451.

[51] N. Darabiha, Transient behaviour of laminar counterflow hydrogen-air diffusion flames with complex chemistry, Combust. Sci. Tech. 86 (1992) 163–181.

[52] F. Contino, H. Jeanmart, T. Lucchini, G. D'Errico, Coupling of in situ adaptive tabulation and dynamic adaptive chemistry:an effective method for solving combustion in engine simulations, Proc. Combust. Inst. 33 (2011) 3057–3064.